OPTIMIZATION OF STEELMAKING PROCESSES IN AN ELECTRIC ARC FURNACE

by

Neel Busa

A Thesis

Submitted to the Faculty of Purdue University

In Partial Fulfillment of the Requirements for the degree of

Master of Science in Mechanical Engineering

Department of Mechanical and Civil Engineering

Hammond, Indiana

May 2023

THE PURDUE UNIVERSITY GRADUATE SCHOOL

STATEMENT OF COMMITTEE APPROVAL

Dr. Chenn Q. Zhou, Chair

Department of Mechanical and Civil Engineering

Dr. Xiuling Wang

Department of Mechanical and Civil Engineering

Dr. Yun Liu

Department of Mechanical and Civil Engineering

Approved by:

Dr. Xiuling Wang

To my parents

ACKNOWLEDGMENTS

I want to start by expressing my sincere gratitude to Prof. Chenn Q. Zhou for her essential advice over the past three years. She has undoubtedly been positioned as a fantastic role model for me in both my personal life and the realm of study. She gave me the chance to attend Purdue University and work at the Center for Innovation through Visualization and Simulation (CIVS), which made me fall in love with and continue to seek a career in research.

Second, I want to thank everyone who served on the committee for the Steel Manufacturing Simulation and Visualization Consortium (SMSVC) and my coworkers at Purdue University Northwest’s Center for Innovation via Visualization and Simulation for their significant contributions to this project. The following people deserve a special note of gratitude for their selfless assistance over the past three years: Dr. Armin Silaen, Dr. Tyamo Okosun, Dr. Yuchao Chenn and Dr. Orlando Ugarte.

Finally, I owe everything to my parents for providing me with all the confidence and support in the world.

TABLE OF CONTENTS

LIST OF TABLES

LIST OF FIGURES

NOMENCLATURE

m_i: Mass of element i

$\dot{m}_{mt}$: Phase mass transfer rate

t: Time

F_{df}: Drag force

F_g: Force of gravity

F_n: Normal component of the contact force

F_t: Tangential component of the contact force

C_D: Drag coefficient

C_P: Specific heat capacity

q: Subscript of phase (liquid or gas)

r_{ij}: Radial distance from particle i to j

D_m: Mass diffusion coefficient

K_{eff}: Effective thermal conductivity

$T_{Liquidus}$: Liquidus Temperature

$T_{Solidus}$: Solidus Temperature

Q_{ht}: Phase heat transfer

Q_{rad}: Rate of radiative heat transfer

Q_{arc}: Arc radiative heat transfer

h: Convective heat transfer coefficient

T_p: Temperature of particle (K)

Nu_p: Nusselt number

D_p: Particle diameter

Pr: Prantel number

Re_p: Particle Reynold’s number

q_{ij}: Conduction heat transfer from particle j to i

T_i: Temperature of particle i

K_r: Rate of reaction of oxidation

τ_{scale}: User defined time scale

ρ: Density

E: Young's modulus

$v_{particle}$: Velocity of particle

v: Poisson's ratio

u_i: Velocity of fluid in i direction

τ: stress tensor

Φ: Phase function

g_i: Gravitational force in i direction

$\bar{v}$: mean velocity

ε: Energy dissipation rate

μ_t: Turbulent eddy viscosity

σ_ε: Constant in turbulence model

σ_k: Constant in turbulence model

$C_{\varepsilon 1}$: Constant in turbulence model

$C_{\varepsilon 2}$: Constant in turbulence model

ABSTRACT

The Electric Arc Furnace is being used quite frequently and significantly in today's environment due to its energy saving and improved product quality features. It is even more important to study more about optimizing the processes involved in the EAF in order to capitalize on its positive features and thus able to contribute to the world in our bid to fight global climate change.

During the refining stage of the Electric Arc Furnace (EAF) operation, molten steel is stirred to facilitate steel/slag reactions and the removal of impurities, which determines the quality of the steel. The stirring process is driven by the injection of oxygen, which is carried out by burners operating in lance mode. In this study, a computational platform is used to analyze the flow dynamics produced during the stirring of the steel bath in an industry-scale EAF. Namely, non-reacting, three-dimensional, transient simulations of the liquid bath stirred by oxygen injection are carried out to analyze the mixing process. The CFD domain includes the liquid bath and the oxygen injected by three coherent jets. The study includes a baseline case, where the oxygen is injected at 1000 SCFM in all the burners. Two sets of cases are also included: first set considers cases where oxygen is injected at a reduced and at an increased uniform flow rate: 750 and 1250 SCFM, respectively. Second set considers cases with non-uniform injection rates in each burner, which keep the same total flow rate of the baseline case, 3000 SCFM. The analysis is also quantified by defining two variables: the mixing time and the standard deviation of the flow velocity. Results indicate that the mixing rate of the bath is determined by flow dynamics near the injection cavities, and that the formation of very low velocity regions or 'dead zones' at the center of the furnace and at the balcony regions prevent the flow mixing. All the non-uniform injection cases reduce the mixing time obtained in the baseline case. The melting of HBI/scrap in an electric arc furnace (EAF) is studied by using a computational fluid dynamics (CFD) platform. A previously developed scrap melting model is extended to investigate the different physical phenomena involved in melting of HBI/scrap charges. The CFD platform merges three computational models, namely a scrap/HBI melting model, an electric arc model and a coherent jet model. The simulation conditions were selected to match those typically seen in industry-scale EAFs.

1. INTRODUCTION TO EAF

1.1 The Electric Arc Furnace (EAF) Manufacturing Process

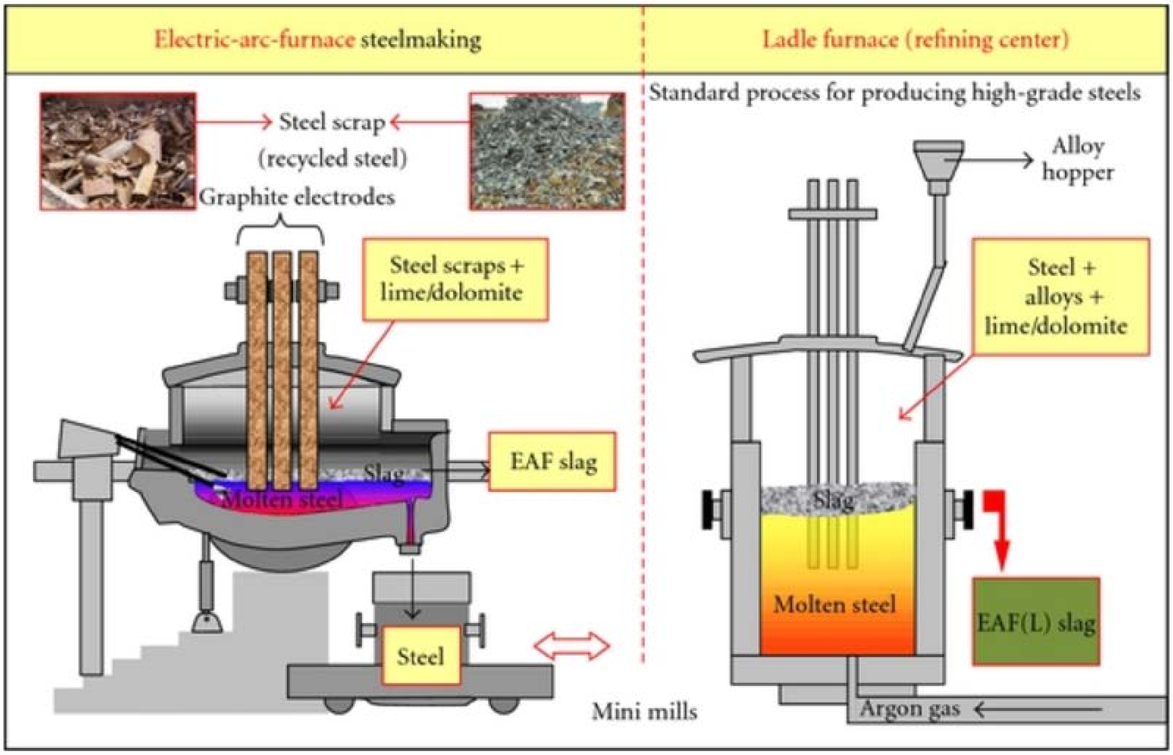

Figure 1. Steelmaking Process [2]

The EAF steelmaking process is one of the major steelmaking methods in the world owing to its high efficiency and utilization of recycled steel scrap material. Steel is the world's second largest commodity after crude oil. This signifies the importance of steel in our day to day lives. Consequently, every ton of steel produced in 2018 emitted on average 1.85 tons of carbon dioxide, equating to about 8% of global carbon dioxide emissions [1]. Steelmakers are increasingly facing a decarburization challenge to achieve the carbon neutrality goals set by 2050.

Global consumption of steel scrap has increased during the past 70 years. A third of the world's steel scrap is consumed by the steel and foundry industries. Due to its great efficiency and low emissions, the EAF has quickly established itself as one of the most important pieces of machinery in the modern steelmaking process. In 2018, the EAF's output of crude steel accounted for 67% [3] of the nation's total production. The EAF steelmaking process is regarded as an energy-intensive process, requiring an average of 1.5 MMBtu of electrical energy per short ton. There are currently about 140 EAFs [3] operating in the United States, and their combined annual electricity consumption is over 8.6 107 MMBtu. In light of this, contemporary EAF research has shifted its attention to improving electrical energy use efficiency, which includes boosting arc performance and minimizing furnace operating costs.

1.2 Significance of the Electric Arc Furnace

According to the findings of an independent study conducted by the London-based CRU Group [3] and published by the Steel Manufacturers Association (SMA), Washington, steel produced by electric arc furnace (EAF) steelmakers in the U.S. has a carbon intensity that is roughly 75% lower than steel produced by traditional blast furnace steelmakers. According to SMA, which represents the EAF steel sector and more than 70% of the steel produced in the United States, it is the largest steel association in the country. The study concludes that recycled scrap-based EAF technology is the sustainable means of steelmaking with regards to the environment as well as quality.

Almost 70% of all steel produced worldwide is made in blast furnaces, which use coal to melt raw materials into iron before turning it into steel. EAF steel is manufactured in steel facilities that primarily use electricity and recycled ferrous waste to build steel, resulting in a lower carbon emission and less energy-intensive process. EAF steel accounts for around 70% of steelmaking in the U.S. The carbon intensity of EAF steelmaking will decrease even further as the U.S. electrical power system continues to be decarbonized thanks to the efforts of utilities and different businesses. Looking forward over the next decade, EAF steelmaking production will be a big winner in the race to produce “green,” “carbon neutral” steel. Another advantage is flexibility: whereas blast furnaces cannot change their output greatly and can run for years at a time, EAFs can be started and stopped quickly. This enables the steel mill to change production in response to demand. Although scrap steel is typically the main feedstock for steelmaking arc furnaces, direct-reduced iron or hot metal from a blast furnace can also be utilized if it is economically feasible.

Figure 2. Regular Size EAF [4]

In comparison to the traditional production method using blast furnaces and the basic oxygen furnace, the electric arc furnace produces steel with fewer carbon dioxide emissions, averaging about 0.6 tons CO_2 for every ton of steel produced.

Theoretically, only low-carbon energy sources like wind, solar, hydroelectric, and nuclear power can be utilized to power electric arc furnaces. This would further lessen the emissions and embodied energy related to the production of steel or any of the several other materials that require furnaces, such as glass. EAFs are therefore a desirable choice for the green industry.

1.3 Stages of EAF Steelmaking

The EAF steelmaking process consists of 4 important stages:

a) Charging - The scrap is loaded into the furnace using an overhead crane from a cylindrical bucket with a drop bottom that is open on top for loading. To provide strong electrical conductivity in the charge, a low danger of electrode breakage, and effective furnace wall protection during meltdown, heavy scrap is cushioned in scrap buckets before being dropped onto the hearth.

b) Melting - The roof is swung back over the furnace after charging, and meltdown starts. The electrodes are configured to bore into the shred layer at the top of the furnace after being placed onto the scrap and striking an arc. To prevent the roof and walls from becoming overheated and being damaged by the arcs, lower voltages are chosen for this early phase of the operation. The voltage can be raised and the electrodes raised slightly to lengthen the arcs and increase power to the melt once the electrodes have reached the dense melt at the bottom of the furnace and the arcs are protected by the debris. This speeds up the formation of a molten pool and lowers tap-to-tap times.

   Whilst EAF development is going toward single-charge designs, once the initial scrap charge has been burned down, another bucket of scrap can be charged into the furnace. To get the appropriate heat weight, the scrap-charging and meltdown process can be repeated as many times as necessary. The number of charges depends on the density of the scrap; denser scrap requires more charges.

c) Refining - The steel chemistry is checked and adjusted during the refining process, which also involves heating the melt above its freezing point in order to prepare it for tapping after all scrap charges have completely melted. In order to remove contaminants like silicon, sulfur, phosphorus, aluminum, manganese, and calcium and their oxides to the slag, more slag formers are added and more oxygen is blown into the bath. Since these elements have a stronger affinity for oxygen, the removal of carbon happens after they have burned out. Nickel and copper, which have a lower affinity for oxygen than iron, cannot be removed by oxidation and must instead be controlled solely through scrap chemistry, such as by adding the previously described direct reduced iron and pig iron.

d) Tapping - When the chemistry and temperature are ideal, the steel is tapped out of the furnace by tipping it into a heated ladle. When slag is discovered during tapping in plain-carbon steel furnaces, the furnace is quickly turned back toward the deslagging side, reducing slag carryover into the ladle. In order to recover valuable alloying elements at the ladle furnace, the slag is also injected into the ladle for some specific steel grades, including stainless steel. Certain alloy additives are added to the metal stream during tapping, and more fluxes, like lime, are placed on top of the ladle to start creating new slag layers.

Frequently, a few tonnes of liquid steel and slag are left in the furnace to generate a "hot heel," which aids in preheating and speeding up the melting of the following charge of scrap. The furnace is "turned around" both during and after tapping. The slag door is cleaned of solidified slag, the visible refractories are examined, the water-cooled components are checked for leaks, the electrodes are examined for damage or lengthened by adding new segments, and the taphole is finally filled with sand. The entire operation will typically take a 90-tonne, medium-power furnace 60 to 70 minutes from the tapping of one heat to the tapping of the next (the tap-to-tap time).

Scrap can be warmed in batch and continuous processes, frequently employing the heat of furnace off-gases, to reduce power consumption. In addition to reducing tap-to-tap time and electrode consumption, scrap preheating to 500° C reduces power consumption per ton by 50 kilowatt-hours [5]. Oxyfuel burners are often used to pre-heat scrap inside the EAF, although this calls for a sizable off-gas system to handle combustion gases. Moreover, electromagnetic coils or permeable refractory blocks for gas stirring are frequently used in furnace bottoms for improved mixing and heat transfer. By utilizing these techniques and the EAF as a scrap melter, power and electrode consumption can be reduced to just 360 kilowatt-hours and three kilograms per ton [5], respectively. The length of the heat is roughly one hour. This indicates that the EAF can get close to the BOF's steelmaking rates by using techniques that were initially created for the basic oxygen process.

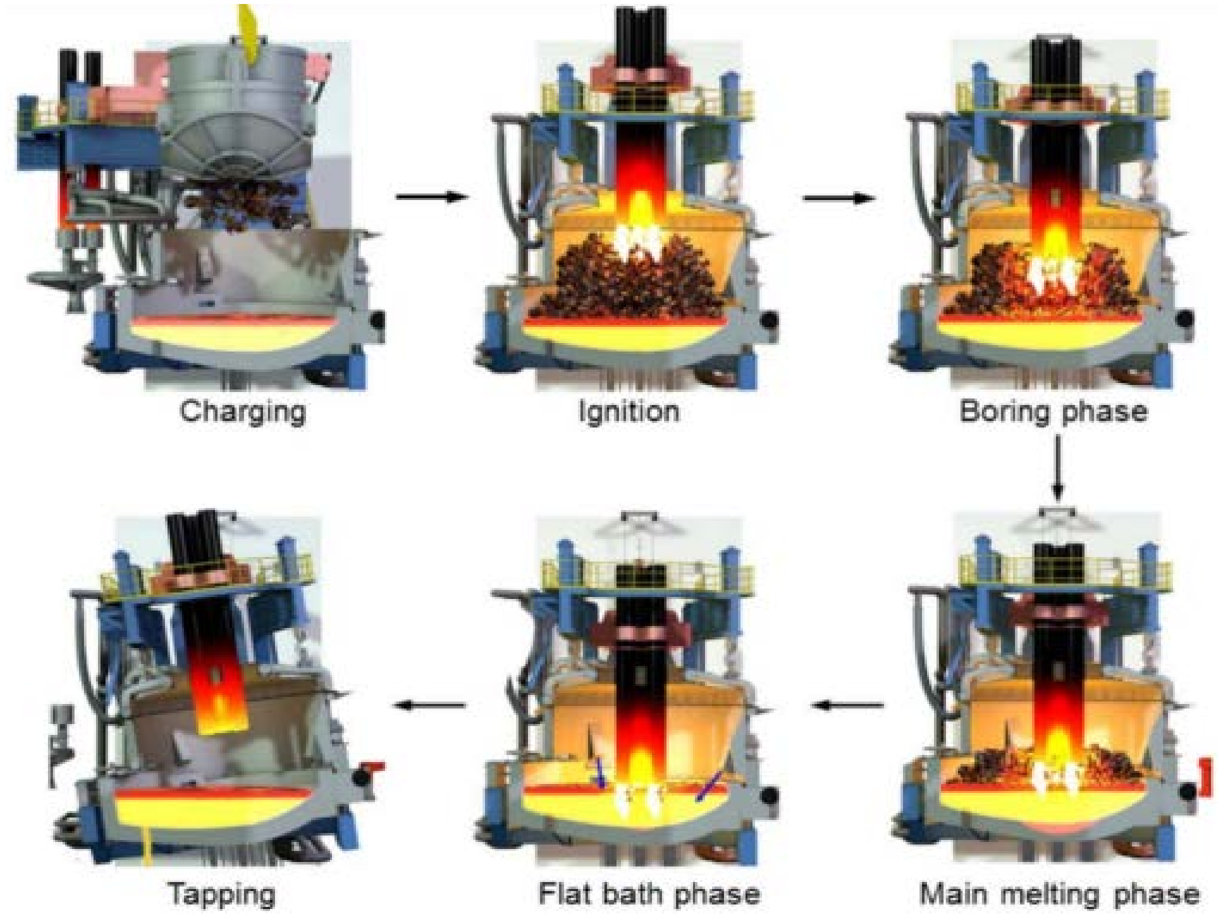

Figure 3. EAF Stages of steelmaking

1.4 Objectives of the thesis

The work mentioned in this thesis is intended to optimize the major EAF steelmaking manufacturing processes. The various projects done for this dissertation are composed of developing and extending a previously developed scrap melting simulator, and application of a steel refining simulator to create impactful analysis for the steel industry. The main research content is as follows:

a) To develop a comprehensive CFD model to simulate melting HBI scrap in an AC EAF along with its steel chemistry and necessary reactions.
b) To perform in-depth analysis in providing sufficient justification for charging HBI scrap instead of traditional scrap to obtain improved finished product as well as reducing energy consumption.
c) To apply a developed steel refining simulator to optimize the refining process and formulate a valid metric to compare mixing efficiency of fluid flow in a flat bath.
d) To study the impact of various factors such as flow rate, different scrap types etc. on the model.

2. LITERATURE REVIEW

The study of the in-bath multiphase flow and the study of the HBI melting process are two general categories for research on the EAF steelmaking process. This chapter starts out with a review of previous studies on steel refining and how the analysis of the mixing efficiency of the bath during refining was used in making a significant improvement to the process.

The second section that follows is a review of the literature on the importance of utilizing HBI as scrap and how it should be accurately modeled using CFD to ensure accurate capturing of its melting phenomena.

2.1 Steel refining stage and Mixing efficiency of a liquid bath

The final stage of the EAF steelmaking process, during which the bath is thermally homogenized and the necessary steel chemistry is attained, is referred to as the "steel refining stage." In order to agitate the molten liquid steel bath, get rid of impurities (such carbon and phosphorus), and further enhance the liquid steel's quality, oxygen is introduced during this time (by foaming). The steel's dissolved carbon will be dissolved by the oxygen, which will be provided by a supersonic coherent jet, and will then react with it to produce in-bath oxygen and CO bubbles, respectively. These bubbles will cause turbulence, which will have a strong stirring impact. In addition to decarburizing the steel, phosphate and silica impurities are also eliminated. High turbulence stirs up the bath and evenly distributes oxygen across the domain, which can be more effectively managed by adjusting oxygen input rates. High-fidelity multiphase computational fluid flow modeling is necessary for this optimization to enhance liquid bath homogenization.

Most studies focus on the refining stage of multiphase fluid flow mixing efficiency research by separating cold flow mixing phenomena from the decarburization events.

Li et al. [7] utilized the volume of fluid (VOF) multiphase model integrated with the discrete phase model (DPM) to describe the gas and liquid two-phase flow in the combined blown converters. The study concluded that the buoyancy-driven bubbles are the driving force behind the majority of the evolved stirring energy in the converter. This application is similar to the phenomenon taking place in the refining stage in the EAF, where continuous blowing of oxygen into the liquid bath forms bubbles and induces stirring. In a chaotic serpentine mixer, the flow and mixing characteristics were numerically examined by Kang and Anderson [8]. Variations in the Reynolds number between 0.1 and 70 were used to investigate the stirring force and mixing effectiveness. The effectiveness of mixing was measured using a parameter known as the intensity of segregation, which was also used to assess how stirring changed over time in the CSM. They came to the conclusion that while inertia doesn't always promote mixing, it does play a significant role in the evolution of the flow profile. Two concentric circular flows that move in opposite directions are produced by a three-dimensional serpentine channel, according to research done by Liu et al. [9]. The experiment demonstrated that significant efficient mixing only happened over a particular Reynolds number threshold.

Moreover, Duan and Wei [10] used coupled side-top blowing to investigate the flow in an argon oxygen decarburization (AOD) converter. By examining the impact of rotating the side blowing gas jet and the impact of changing the blowing volume, the characteristics of fluid mixing were examined. The findings suggest that rotating the gas jet while maintaining the same blowing volume increases agitation and improves mixing efficiency. Lang et al. [11] examined how a static mixer mixes its contents. According to the study, the key factor for the fluid to be thoroughly mixed is the vortices produced by the turbulent flow in the mixer. Mazumdar and Guthrie's work [12] examines mixing in gas-stirred liquid baths for a ladle. The study establishes that mixing is a result of both eddy-diffusion processes and convection, which occur during the turbulent bath stirring. To examine mixing events in a gas-stirred ladle, Zhu et al. [13] combined mathematical modeling with an experimental water model. They came to the conclusion that the position and angle of blowing have a significant impact on fluid movement in the bath. While determining the flow's mixing time, the tracer's position is also crucial. Amaro-Villeda et al. [14] investigated how slag characteristics affected mixing time. The top layer of the liquid bath consumes a certain amount of stirring energy depending on the nozzle configuration and gas flow rate, as well as the properties of the slag such as viscosity. This formula serves to derive a simplified method of modeling the slag and helps to calculate the energy lost to the slag layer. The parameters of gas agitation in a side blowing ladle and its impact on fluid flow were examined by Cheng et al. [15]. He came to the conclusion that the uniform velocity distribution throughout the entire domain and the flow's agitation power work together to impact mixing time. Shorter mixing times are a result of these characteristics working together with decreased stationary region rates.

According to Chen et al. [16], bubble stirring is important to the EAF refining process and considerably increases homogenization of the molten steel bath. Research was done on mixing and flow patterns in micro-channels by Jayaraj et al. [17]. An empirical formulation to determine the mixing efficiency of a specific micro-channel was developed using design configurations of different micro-channels to examine their impact on mixing. Although mixing in micro-channels differs greatly from mixing in macro-devices, the same measurement concepts can be utilized in both situations. Li [18] examined the bottom stirring mixing procedure in an electric arc furnace. Results demonstrate that off-center blowing of gas into the liquid bath lead to increased stirring intensities and better velocity distribution throughout the domain. The diameter and location of plugs were employed as a function of the mixing duration for the flow.

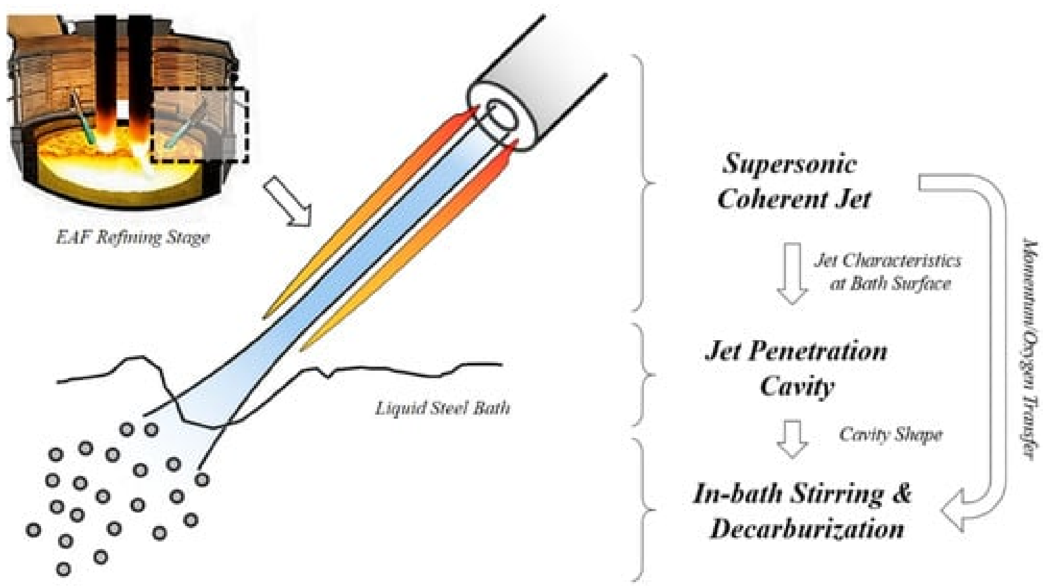

Figure 4. Oxygen blowing during refining

Although the aforementioned research quantifies the metrics for mixing and homogenization in a liquid bath, there is currently insufficient proof to establish the ideal parameters for gas insertion. This study's objective is to identify the factors that contribute to the stirring process's optimization by analyzing the flow features produced by various injection flow conditions in an industrial-scale

EAF. This contributes to the efficient use of energy and has a direct impact on the final steel product's quality. The decarburization process proceeds more quickly the more evenly distributed the carbon is inside the bath. To ascertain the impact of the oxygen injection rate into the liquid bath, a parametric study is conducted in this experiment. Also, certain measures have been put forth to quantify the degree of mixing and contrast the domain's flow characteristics depending on these measurements. While it focuses on the flow dynamics that regulates the mixing process in the liquid steel bath, this study does not take species reactions into account.

2.2 HBI as a scrap and its melting characteristics

In order to combat rising productivity costs, battle carbon footprint reduction, and produce high-quality goods, steelmakers have turned to other sources of trash. HBI/DRI has becoming more popular as a replacement for conventional scrap as a result.

A compacted version of DRI, hot briquetted iron (HBI), is created with certain, dependable chemical and physical properties. HBI is made to be melted in a variety of iron and steel processes and delivered across long distances. Unlike scrap, which often has a collection season, it is accessible all year long. The manufacturer certifies the chemical make-up of HBI, and ISO quality standards are closely adhered to. Most often, physical traits are held responsible for the development of HBI. The furnace slag layer can be quickly penetrated thanks to its increased mass. HBI will pick up 75% less water and is 100 times more resistant to re-oxidation than traditional DRI. HBI also results in fewer fines, which increases value for users and lessens handling and shipping safety concerns. HBI can be batch charged or constantly fed to a melting furnace since it can be handled by typical materials handling equipment due to its size and shape.

The species and carbon reaction required to compute the melting of HBI/scrap charges under conditions found in the operation of industry-scale EAFs are added to an earlier developed CFD scrap melting platform [20] in the current study.

Figure 5. HBI Pellets [19]

Gonzalez et al [21] used a numerical method to model the melting of DRI in an EAF. Three sub-models made up the computational platform: an arc model, an Eulerian fluid model, and a Lagrangian melting model. By infusing tiny DRI particles at high temperatures, this method verifies the functionality of the process. The study comes to the conclusion that the frozen shell period, which makes up over 50% of the melting duration, has a significant impact on the rate of DRI melting. Correlations discovered through research carried out to examine the melting rate of briquettes are reported by Caffery et al. in [22]. The bath carbon content affects the CO evolution rate, which in turn affects the melting rate of the HBI, according to an inverse heat transfer analysis created for this work. The melting procedure of DRI is described in detail by Dutta and Sah [23]. The chemical reduction of oxygen from the iron impacts the quality of the steel produced, hence the authors recommend using iron ore pellets with a high iron content, low gangue concentration, and are easily reducible. The reaction kinetics of each of the various processes involved in the melting of DRI were published by Morales et al. in their publication [24]. According to the study's findings, the pace at which iron oxide is reduced is the most important factor in the procedure and affects the melting profile of the scrap dynamically. In order to make steel, HBI DRI pellets' melting behavior was given by Kiasaraei [25]. He measured the rate of decarburization using experimental data and investigated the impact of pellet preheating and beginning carbon content on the reaction rate. Conclusion: Preheating primarily affects the pace of reaction of FeO and carbon inside the pellet, whereas carbon content had a more significant impact on the kinetics of both phases. Based on data, Kirschen et al. [26] advise improving the DRI melting process by comparing the slag composition of DRI charges with those of steel scrap charges. The authors came to the conclusion that carbon injection and less overall slag mass result in an effective reduction of FeO. A flowchart was presented by Alameddine and Bowman [27] to precisely model the melting of DRI in an EAF. By evaluating the amount of energy needed to produce one kilogram of DRI depending on key factors including carbon content and degree of metallization, the study aids in determining the thermal efficiency of the model. According to Anderson [28], the proper composition of the DRI feedstock is necessary for effective DRI utilization. Operating procedures should be adjusted based on DRI chemistry since DRI-containing carbon is a more effective carbon source than charged or injected carbon.

For the investigation of the HBI DRI melting process, the aforementioned research offers solid precedents. Little study has been done on explicitly modeling and simulating this phenomenon at an industry scale, though. It takes a lot of numerical stability to precisely describe the processes that take place during the physical melting of the solid phase into the liquid phase. In this study, a thorough CFD platform that was previously used to model the melting of scrap in an EAF operation is expanded to model EAF situations where scrap and HBI materials are fed into the furnace. This study specifically examines the melting rate that arises from incorporating HBI into the process, and the findings are contrasted with those from a 100% scrap charge case. The analysis also explains how HBI affects the electrodes' bore-in and how heat is transferred inside the furnace. The many scenarios used in this analysis aid in identifying the circumstances that increase the effectiveness of the HBI/scrap usage in the EAF operation.

3. FLUID FLOW AND DECARBURIZATION OPTIMIZATION OF THE STEEL REFINING STAGE

3.1 Introduction

The steel refining stage in the EAF steel manufacturing process, is very essential to the quality of the final product. In this stage, the molten steel obtained from melting of the scrap, is further refined to obtain the desired steel chemistry of the product manufactured.

This simulator is broken down into 3 stages, to simplify the problem of high computation costs and instability of numerical physics in calculating a supersonic coherent jet interacting with a liquid steel bath. The three stages involved are as follows:

a. Simulating a supersonic coherent jet in open space. This simulations helps in obtaining important variables such as velocity, oxygen content of the jet reaching the liquid bath.
b. The next stage includes calculating the cavity formed on the liquid surface due to the impact of the high momentum jet, using these variables. The cavity is assumed to be a paraboloid and also has a particular depth, based on the momentum imparted to the liquid.
c. The final stage corresponds to using this cavity modelled along with the bottom section of an EAF, to be used as a physical boundary, to inject oxygen into the liquid. This injected oxygen creates a stirring effect and aids in thermally homogenizing the liquid bath.

This particular methodology breaks down the complexity of the phenomenon furthermore helps in investigating important factors which lead to optimization of the refining process. This model has been previously developed by my mentor Yuchao Chen and validated via plant trials conducted with Steel Dynamics Inc. (SDI).

The current study focuses more on application of this model and utilizing it to analyze the flow during the refining stage in depth and innovating strategies to improve the decarburization efficiency of several steel manufacturing plants. Data used for this study is in collaboration with EVRAZ North Americas and the customized objectives of this study are:

a. Flow and thermal homogenization of liquid flow in domain
b. Developing metric to compare mixing efficiency of a flow
c. Optimizing rate of decarburization during refining

The assumptions used for this project are:
a. No reactions occurring between the liquid and the supersonic jet
b. Slag not considered to be part of physical domain, but properties of slag used for calculation of cavity design
c. No slip walls

3.2 Numerical Models

3.2.1 Governing Equations

As mentioned, the first step is to simulate the supersonic coherent jet in an open space under furnace conditions. The coherent jet injection is solved as compressible, non-isothermal, steady state flow. The solver used is a compressible solver implemented in ANSYS Fluent version 2019. The continuity equation solved for the coherent jet is given by:

$$\nabla.(\rho\vec{v}) \tag{1}$$

The momentum equation is constructed as:

$$\nabla.(\rho\vec{v}\vec{v}) = -\nabla p + \nabla.(\bar{\bar{\tau}}) + \rho\vec{g} + \vec{F}, \tag{2}$$

where ρ, $\vec{v}$, p, $\bar{\bar{\tau}}$, g and $\vec{F}$ are the density, velocity vector, static pressure, stress tensor, gravity acceleration and the external body force, respectively. Moreover, the energy conservation equation can be written as

$$\nabla.[\vec{v}(\rho E + p)] = \nabla.\left[\left(k + \frac{c_p.\mu_t}{Pr_t}\right)\nabla\mathrm{T} - \sum_j h_j\vec{J_j} + (\bar{\bar{\tau}}_{eff}\,.\vec{v})\right] + S_h, \tag{3}$$

Here, E, k, c_p, and μ_t are the total energy that corresponds to the sensible enthalpy h, thermal conductivity, specific heat, and turbulent viscosity, respectively. Pr_t is the turbulent Prandtl number whose default value is 0.85 for the $k - \varepsilon$ turbulence model, $\vec{J_j}$ is the diffusion flux of substance j. S_h is the volumetric heat source, which includes the heat of chemical reactions. The turbulence viscosity is modelled as:

$$\mu_t = C_\mu \rho \frac{k^2}{\varepsilon}, \tag{4}$$

where the constant is modified in order to include the influence of entrained ambient gas [14] (which improves the prediction of the jet potential core length) as

$$C_\mu = \frac{0.09}{C_T}. \tag{5}$$

The modification of the turbulent viscosity is loaded into the CFD software via a User-Defined Function (UDF) code. Figure 1 shows the interaction of the coherent jet with the liquid bath. This interaction will generate a cavity in the surface of the liquid steel, which is computed in the second step of the CFD setup.

For the second step, a cavity is estimated on the surface of the liquid bath based on the impingement of the supersonic jet on the bath [29]. The jet momentum transfer and oxygen delivery are calculated in this study to estimate the cavity shape and size. Based on the energy balance calculation, the momentum transferred by the jet flow to the liquid steel can be calculated as:

$$P_{s,avg} = \alpha \rho_{O_2} {v_{O_2}}^2 A = \frac{\alpha \rho_{O_2} A}{\rho_s} \left[\frac{1}{\Delta z} \int_{z2}^{z1} v_{O_2}(z) dz\right]^2 \tag{6}$$

The amount of deliverable oxygen from the jet to the liquid bath is expressed as:

$$m_{O_{2,avg}} = \frac{1}{\Delta z} \int_{z2}^{z1} m_{O_2}(z) dz \tag{7}$$

About 6% of the momentum is transferred from the jet to the bath due to dampening effects of the slag layer and viscosity effects [16]. By separating the process into two simulations, one for the coherent jets and one for the refining model, the computational cost is significantly reduced, as the compressible solver is needed only for the coherent jet model, which is a small section of the EAF domain. The jet cavity design is integrated into the refining simulation, with the cavity being part of the boundaries of the EAF domain. The main characteristics needed from the coherent jet simulation are the velocity of the jet reaching the bath and the amount of oxygen reaching the bath. The shape of the cavity is assumed to be a 3D paraboloid which follows the mathematical expression:

$$z = \frac{(x^2+y^2)}{c}, \tag{8}$$

c is the constant needed to be defined by a given volume and depth of the cavity. The volume of the cavity [30] can be obtained by:

$$V = \frac{\pi \rho_j {v_j}^2 {d_j}^2}{4 g \rho_s}, \tag{9}$$

where ρ_j and ρ_s are primary densities of jet and liquid steel, v_j and d_j and jet velocity and jet diameter of nozzle respectively. The jet penetration depth is an empirical formula derived by Ishikawa et al. [32] which described mathematically the indentation created by the coherent jet in the liquid bath. This is expressed as:

$$D = \gamma_{h_0} e^{-\frac{\sigma_1 L}{\gamma_{h_0} cos\theta}} \tag{10}$$

$$\gamma_{h_0} = \sigma_2 (\frac{\dot{V}}{nd\sqrt{3}}) \tag{11}$$

Here, L is the distance between nozzle exit and bath, σ_1 and σ_2 are 2 constants equal to 1.77 and 1.67, derived from an experiment analysis [32].

Considering the chemical reactions that take place in this simulation, the oxidation of carbon, which is known as the decarburization reaction, takes place in cells of the domain that contain oxygen. The amount of oxygen limits the rate of the reaction and is given by:

$$-\frac{W_s}{100\, M_c} \frac{d[\%C]}{dt} = \frac{2 n_c Q_{o_2}}{22400}\ x_c \tag{12}$$

3.3 Methodology and Computational domain

The computational model utilized for this investigation is briefly described in this section. The reader is directed to [11] for more details, including specifics on the model validation and the installation of the CFD platform.

The model performs computations in three steps while setting up the domain's physical boundaries. Three main physical processes that occur simultaneously during EAF refinement are used to characterize these three stages: oxygen blowing into the liquid bath via co-jet burners; interaction between the coherent jet and the liquid steel; and bath churning brought on by high intensity jet injection. This methodology helps with the control and analysis of important parameters while guaranteeing the simulation accuracy of the refining stage without sacrificing compute resources. Two simulations—the coherent jet model and the refining model—completed by two distinct CFD platforms are used to calculate these three processes. The following steps are taken in order to finish the entire EAF refining process utilizing these two solvers:

1. The supersonic coherent jet is simulated first based on the injection conditions of the burners operating in lance mode. The key parameters obtained from this simulation are the velocity profile of the jet, from the tip of the burner to the surface of the bath, and the oxygen mass fraction profile for the same.
2. Outputs from the coherent jet simulation are used to estimate the cavities formed by the jets on the surface of the liquid bath, according to equations given by Chen et al. [11].
3. The computational domain for the refining simulation is created. This domain includes the liquid bath only. The cavities computed in step 2 are included at the top boundary of the domain, which is the surface of the steel bath. The refining simulation is launched, and oxygen is injected at the cavities at the rate provided by the coherent jet simulation solution.

The oxygen injection's velocity stirs the solution and propels the mixing of contaminants like carbon and metal oxides. The simulations in this work presume that the bath only contains a single species of steel, despite the fact that the refining model is capable of computing numerous species and reactions; hence, reactions in the bath are not computed. The key equations obtained at each of the aforementioned steps are then described in more detail.

The computational domain used for this simulation is the bottom section of an EAF. This sections is specifically chosen as once the solid scrap is melted, the liquid steel flows to the bottom of the furnace.

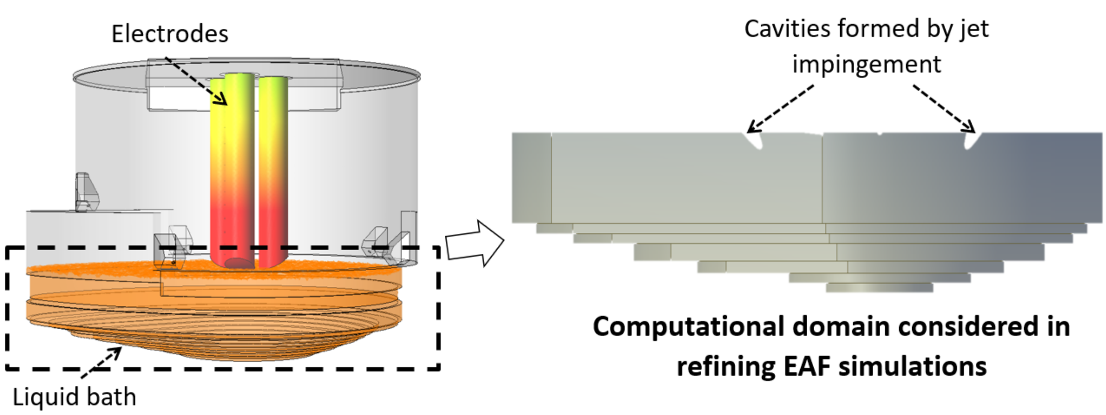

Figure 6. Computational domain of the EAF

The simulation incorporates the solution of the Navier-Stokes equations into a finite volume scheme by using the ANSYS Fluent platform. Specifically, the computational solution is based on an Eulerian multi-phase, incompressible approach, where the primary phase is the molten liquid and the secondary phase is the injected oxygen.

The size and shape of the cavity vary according to the velocity of the jet reaching the bath, the diameter of the burner nozzle and the density of the liquid bath. As expected, the model predicts a cavity with larger volume and deeper penetration depth as the jet velocity increases. Figure 7 shows the cavity formed in three scenarios, where the injection rates are 750, 1000 and 1250 SCFM.

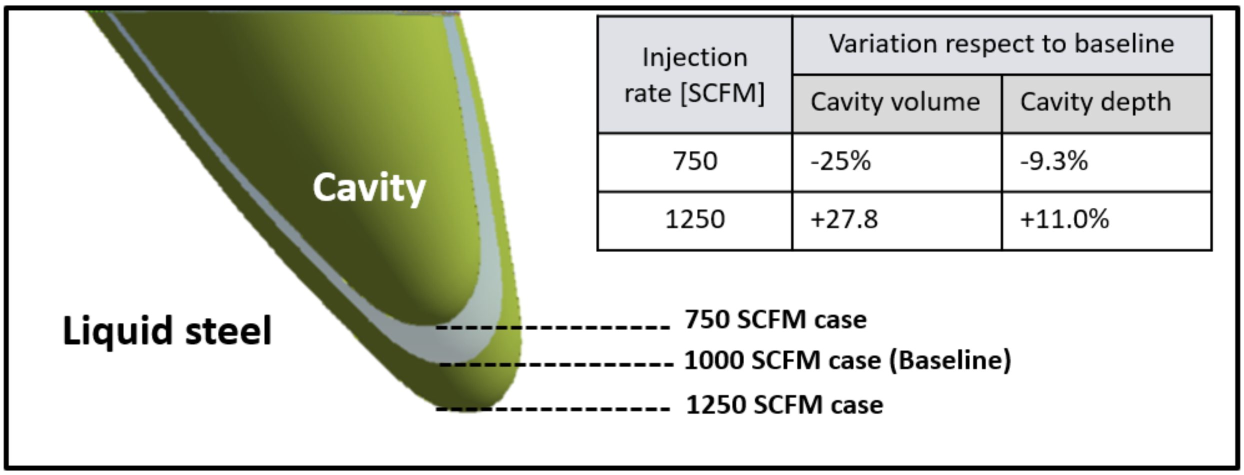

Injection rate [SCFM]	Variation respect to baseline	
	Cavity volume	Cavity depth
750	-25%	-9.3%
1250	+27.8	+11.0%

Figure 7. Cavity formation on surface of bath

The boundary conditions for the baseline simulation, were calculated for 3 coherent jet burners with each having a 1000 SCFM (standard cubic feet per minute) flow rate, of oxygen injection. The baseline simulation for this research considers industrial EAF operation conditions provided by EVRAZ North America. The simulation setup includes two phases. The primary phase is assigned to the gas and the secondary phase is assigned to the liquid. In the simulations, the gas corresponds to oxygen and the liquid to molten steel. The parameter values used in the baseline case are listed in Table 1

Table 1. Parameters used for the baseline refining simulation

Name	Variables	Value
Jet cavities	Quantity	3
Oxygen injection	Flow rate (in all three burners)	1000 SCFM
	Mach number	2.1
	Mass fraction of oxygen	100%
Liquid Steel	Density	7500 kg/m^3
	Static temperature	1890 K
Coherent jet burner	Angle of inclination	45 degrees

3.4 Baseline Case results

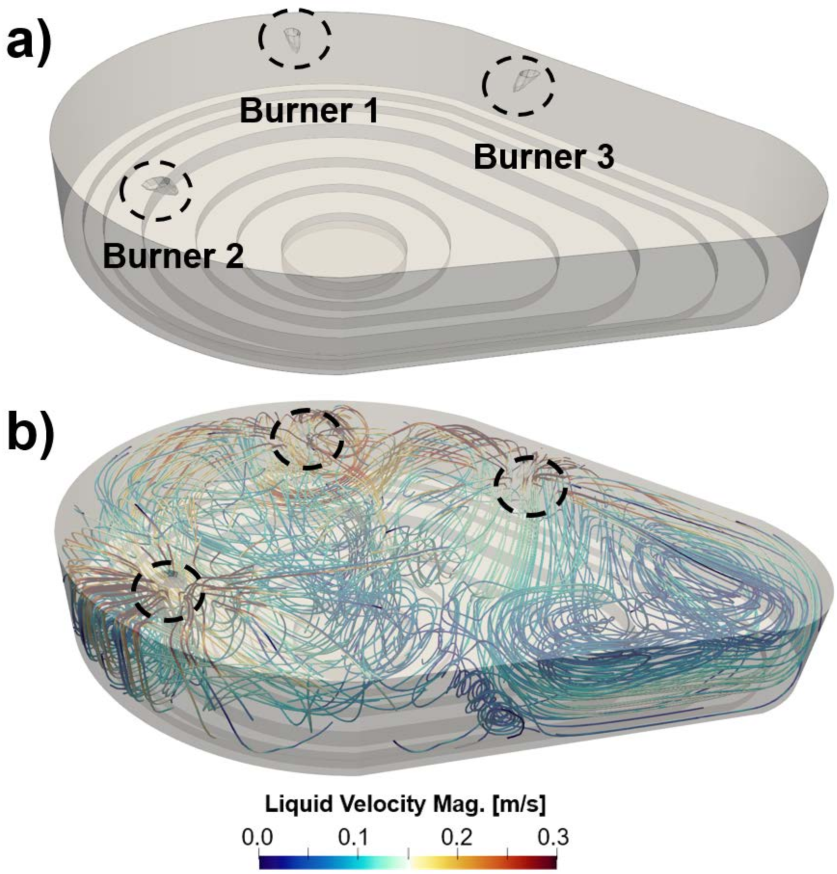

Figure 8. Burner Locations and flow patterns at 600 s

The baseline case considers oxygen injection at a rate of 1000 SCFM in all the burners, which operate in lance mode. Figure 8 shows the location of burners in Figure 8a and the flow patterns associated to such injection rates after 600 s in Figure 8b. The flow pattern shows large fluid velocities near the burners, dropping significantly as the flow changes directions due to interaction with the walls and the flow injected from adjacent burners. Overall, the flow velocity magnitude decreases from around 5 m/s to 0.1-0.5 m/s range. The flow pattern is particularly non-uniform. The main reasons are the geometry of the furnace, the asymmetric distribution of the injectors and the angle at which the injection is produced.

Figure 9 shows the instantaneous velocity magnitude at a plane located 0.5 m. from the top of the domain. The velocity contours are computed at t = 200 s, 400 s and 600 s. The contours include, in addition, the velocity vectors of the flow field. Figure 9a through 9c shows that the flow field does not change significantly along these time intervals. At all times, the flow velocities are larger near burner 1, as a result of the interaction of burners 1 and 3. On the contrary, the flow injection near burner 2 decays quickly as this is the only injection point on the lower side of plane 1. Flow recirculation is shown at burner 1, and adjacent to burners 2 and 3. Also, the flow velocity near the balcony of the furnace (right end of plane 1) approaches zero, which determine a ‘dead zone’ of the flow. Low velocity regions or ‘dead zones’ are also formed at the lower wall of the plane (at the region opposite to burner 3), near the center of the domain, and near burner 2. These flow features are consistent along the three times shown in Figure 9.

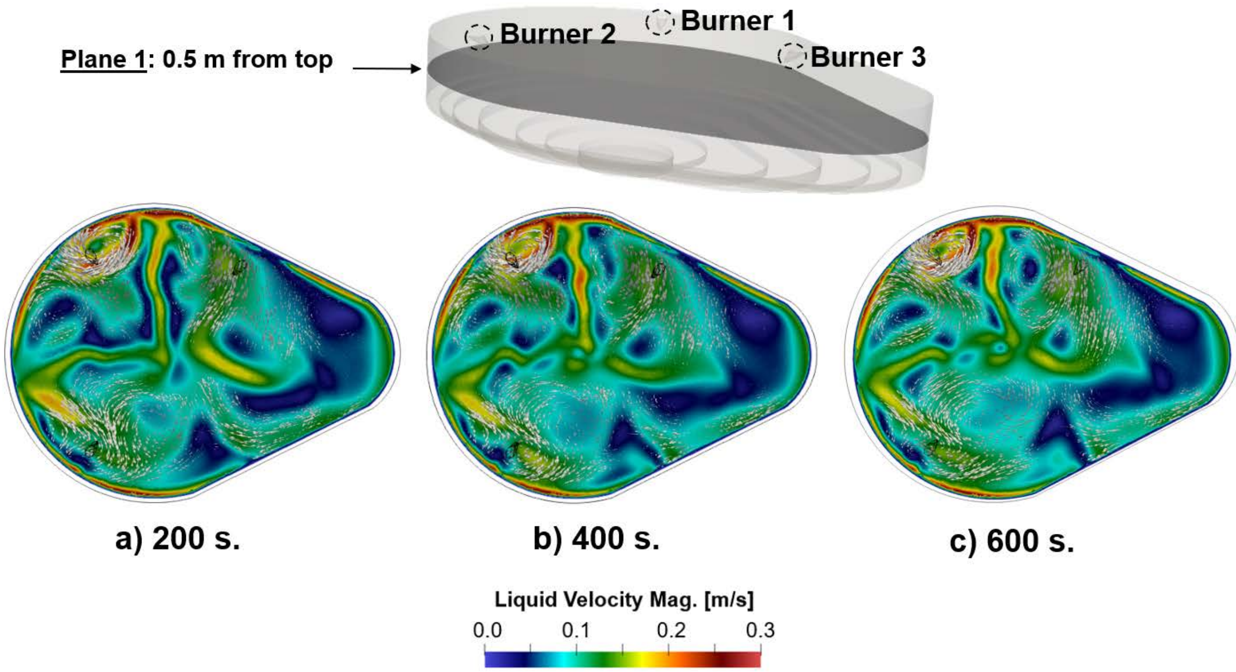

Figure 9. Time evolution of velocity magnitude and flow vectors near the bath surface in baseline case

Figure 10 shows the instantaneous velocity magnitude and flow vectors of the liquid steel at three planes. The locations of the planes are shown on the top of the figure. These results correspond to t = 600 s. of flow simulation. As expected given the source of fluid momentum, the flow intensity is larger near the top of the domain. The main features observed in plane 1 (Figure 10a) are also seen in plane 2 (Figure 10b). Namely, large velocities develop near burner 1 and at the upper side of planes 1 and 2, towards the left end. Plane 2 is taken further inside the furnace (Figure 10b) and, overall, it shows reduced velocities as compared to plane 1. The flow intensity is further reduced in plane 3, taken 1.2 m from the surface of the liquid bath. In plane 3 the velocity magnitude does not exceed 0.2-0.25 m/s, although recirculation patterns similar to those observed in planes 1 and 2 are maintained.

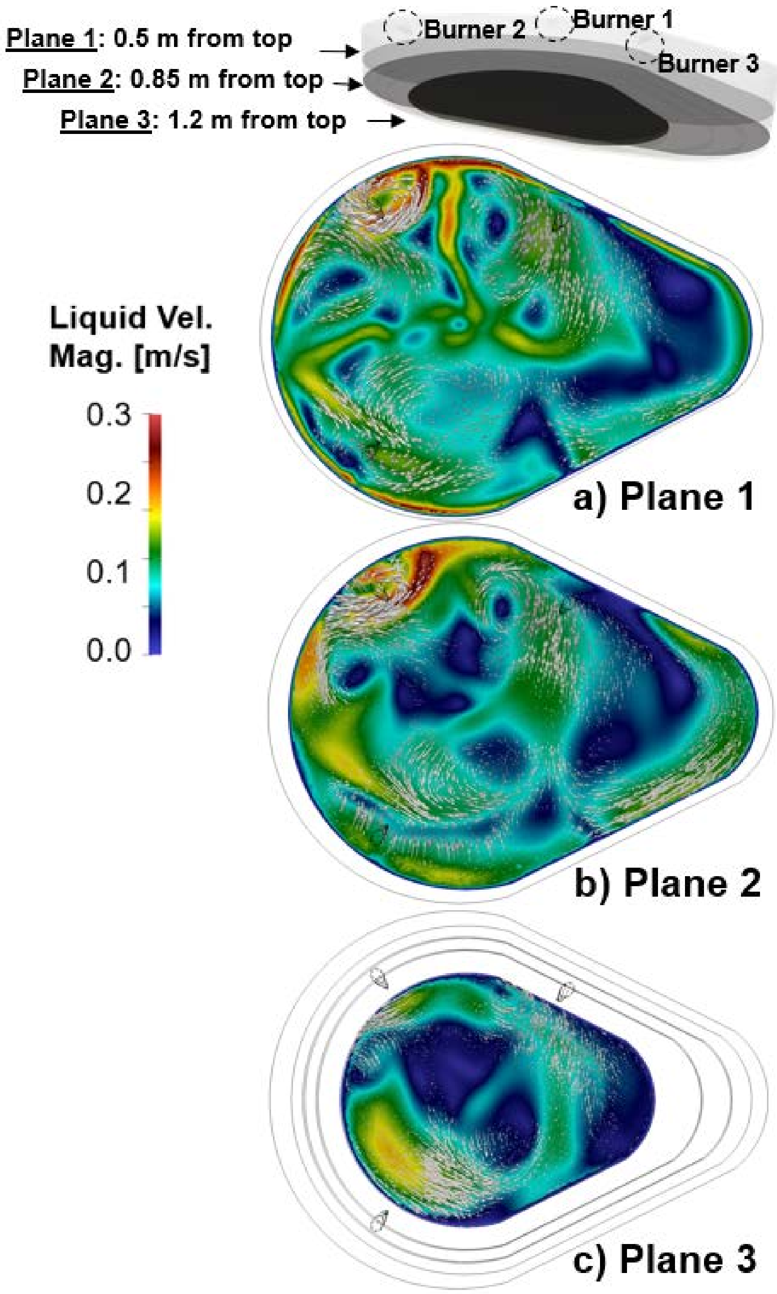

Figure 10. Velocity magnitude and flow vectors computed at multiple planes in baseline case

Figure 11 further extends the analysis by considering two vertical planes, which are shown at the top of the figure. Figure 10a shows plane 4, which is taken towards the balcony of the furnace. Plane 4 shows larger liquid velocities at the left side, near the locations of burners 1 and 2. The flow vectors on the left side of plane 4 show a vertical recirculation produced by the interaction of the flow injected at burners 1 and 2 with the bottom of the furnace. Therefore, the asymmetric distribution of the burners at the top of the liquid bath leads to the formation of recirculation structures in the horizontal and vertical direction near burners 1 and 2, as shown in planes 1-3 (Figure 10) and plane 4 (Figure 11a). Figure 11b shows larger flow velocities near burners 1 and 3, although the recirculation pattern in this plane is weaker than in plane 4.

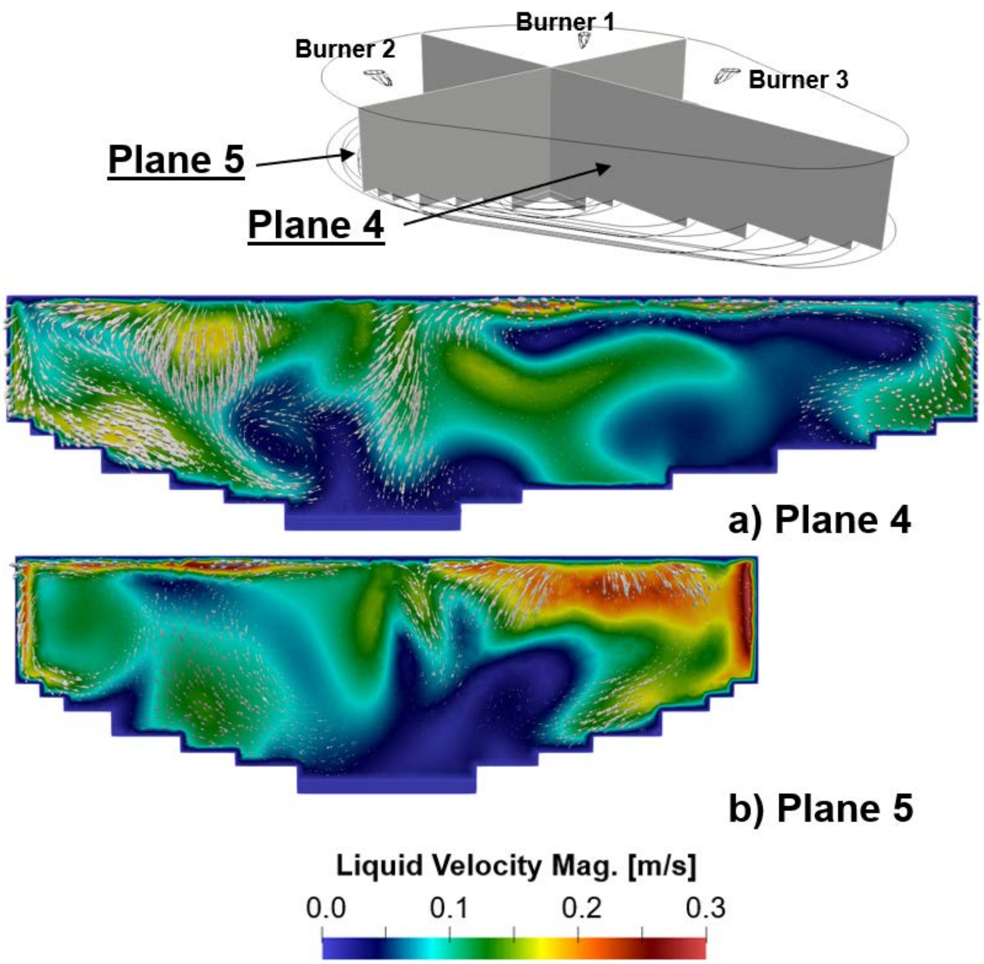

Figure 11. Velocity magnitude and flow vectors computed at vertical planes in baseline case

Figure 12 shows the instantaneous velocity components *u*, *v* and *w* of the liquid steel at planes 1, 2 and 3 discussed earlier. The axis orientation is included at the bottom left of the figure. Figures 12a and 12b show that the flow intensity is larger at the left side of the planes, near burners 1 and 2. Figure 12b shows that *u* and *v* increase as the flow interacts with the end wall at the balcony. The *w* contour in Figure 12a shows the flow structures produced vertically as a result of the flow injection. Namely, the flow injection produces the stirring of the liquid bath upwards. The *w* contours in Figure 12a also shows negative velocities associated to the stirring, which determine the recirculating patterns seen in planes 4 and 5 at Figure 11. The overall intensity of flow vertical penetration decreases as we move into the liquid bath, and it is seen much reduced *w* contour at the furnace bottom in Figure 12c.

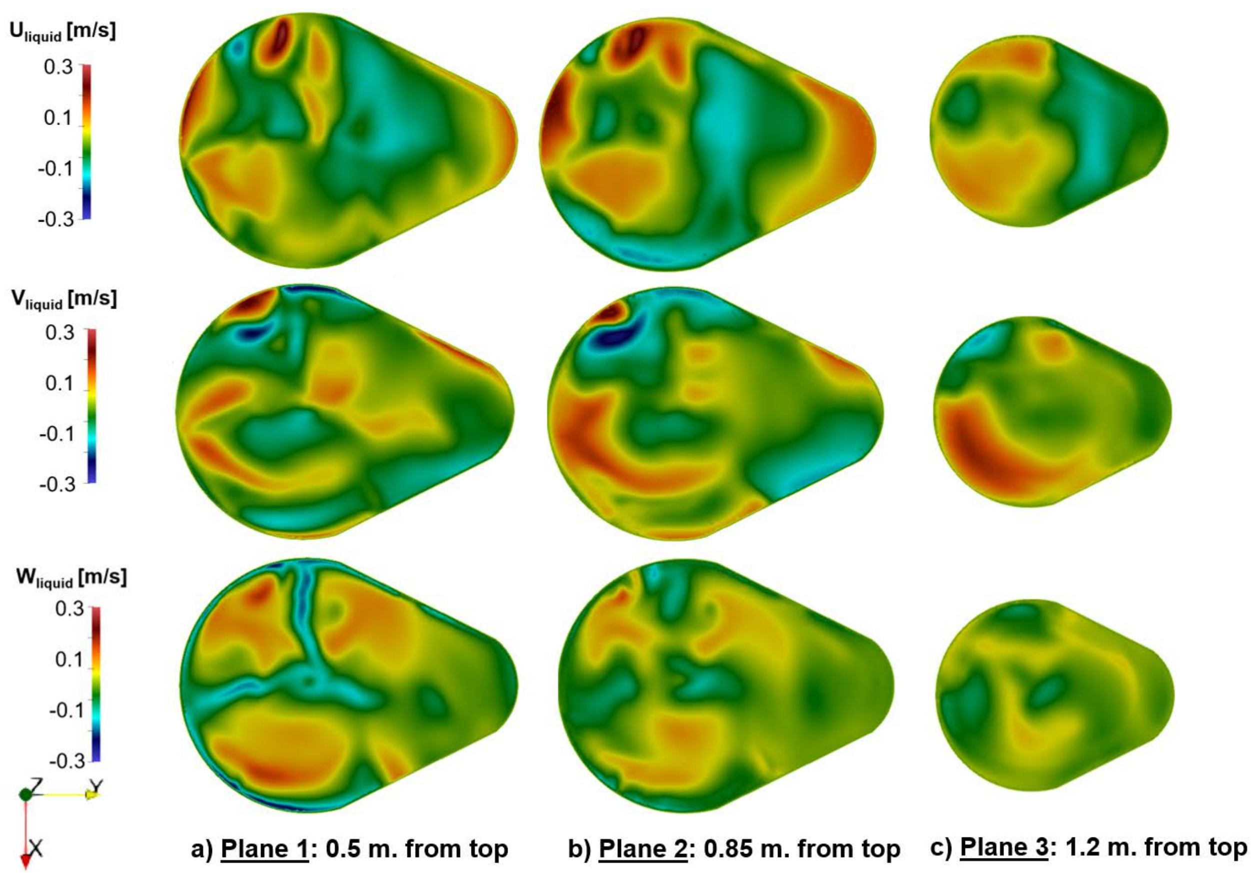

Figure 12. Velocity components computed at multiple planes in baseline case

3.4.1 Impact of Uniform burner flow rate

The effect of both increasing and decreasing the flow rate of the burners is explored in this section. Specifically, two additional cases are completed where the flow rates at the burners are uniformly increased 25% and decreased 25%. These are listed in Table 2 as cases 2 and 3, respectively. It should be noticed that coherent jet burners are designed to operate at a range of 20%-30% of their factory set flow rate, as this helps maintain the stability of the flame, and preserves maximum oxygen delivery to the bath.

Table 2. Case conditions for Uniform flow rate parametric study

Cases	Coherent jet flow rates [SCFM]			Notes
	Burner 1	Burner 2	Burner 3	
1	1000	1000	1000	Baseline
2	1250	1250	1250	Increased flow rate
3	750	750	750	Decreased flow rate

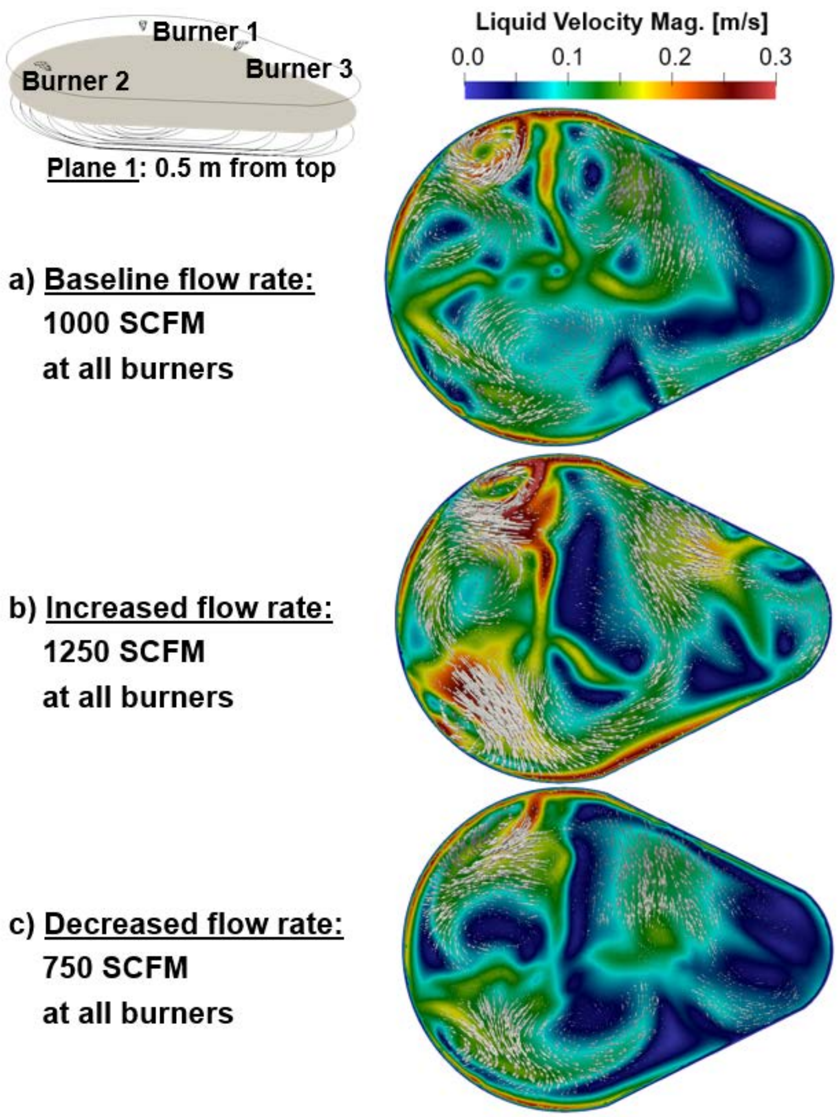

Figure 13. Velocity magnitude and flow vectors of baseline and cases with increased and reduced flow rates at t = 600 s.

The effect of increasing and decreasing the flow rate in the burners are shown in Figure 13, where these scenarios, in addition to the baseline case, are compared at t = 600 s. Figure 13b shows that the increased flow rate case intensifies the flow near the burners, and leads to the formation of a 'dead zone' at the center of the furnace, where the flow velocity is negligible. The flow vectors in Figure 13b show a significant increase in the liquid velocity near burners 2 and 3, and near the walls, as compared to the baseline case. Figure 13c shows the case with decreased flow rate. Here, the flow velocities are reduced throughout the domain, and the dead zone regions are the largest among the three scenarios.

In addition to the impact of the modified injection rates on the velocity magnitudes, changes on the injection rates also modify the flow patterns, reflected on the location of the recirculation zones and the formation of the dead zones. Figure 14 compares the three cases listed in Table 2 by computing the velocity magnitude at a plane taken along the centerline of the furnace, as shown at the top of the figure. Figure 14b shows that the increased flow rate case moves the recirculation region towards the left side of the plane, and makes the ‘jet’ type flow in the center of the domain (along the depth of the EAF) stronger than in the baseline case. The increased flow rate case strengthens the two vortices at the left side of the jet-type vertical flow. On the contrary, as the flow rate is reduced in all the burners from 1000 to 750 SCFM, one vortex is observed near the left wall of the plane, and the flow penetration towards the bottom of the furnace weakens significantly (Figure 14c).

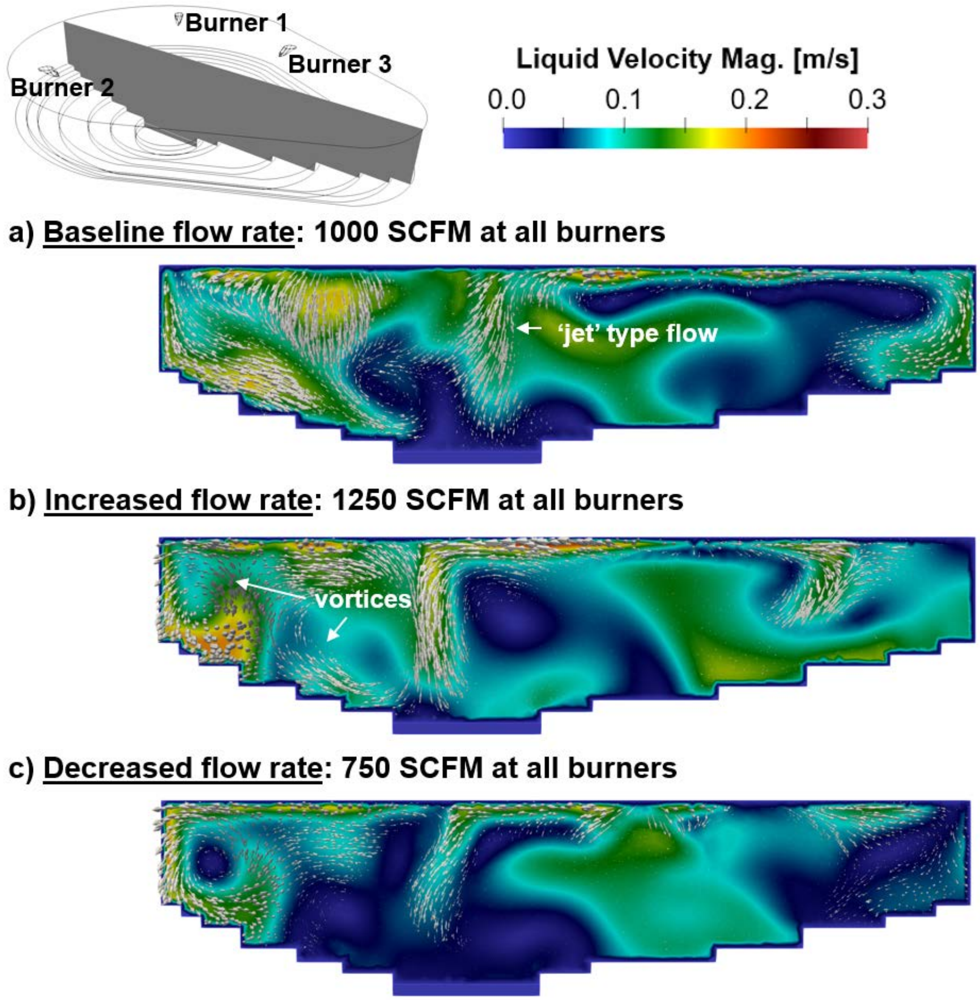

Figure 14. Velocity magnitude and flow vectors of baseline, increased and reduced flow cases computed in vertical planes

Figure 15 shows regions in the furnace domain where the instantaneous velocity magnitude is larger than 0.15 m/s for the baseline case and for the cases with increased and reduced flow injection rates. These regions confirm the highly asymmetric distribution of the flow velocities, as the larger velocities are obtained at the half part of the domain that contains burners 1 and 2. Figure 15b shows that by increasing the flow injection from 1000 to 1250 SCFM, the regions containing velocities above 0.15 m/s extends towards the balcony of the furnace.

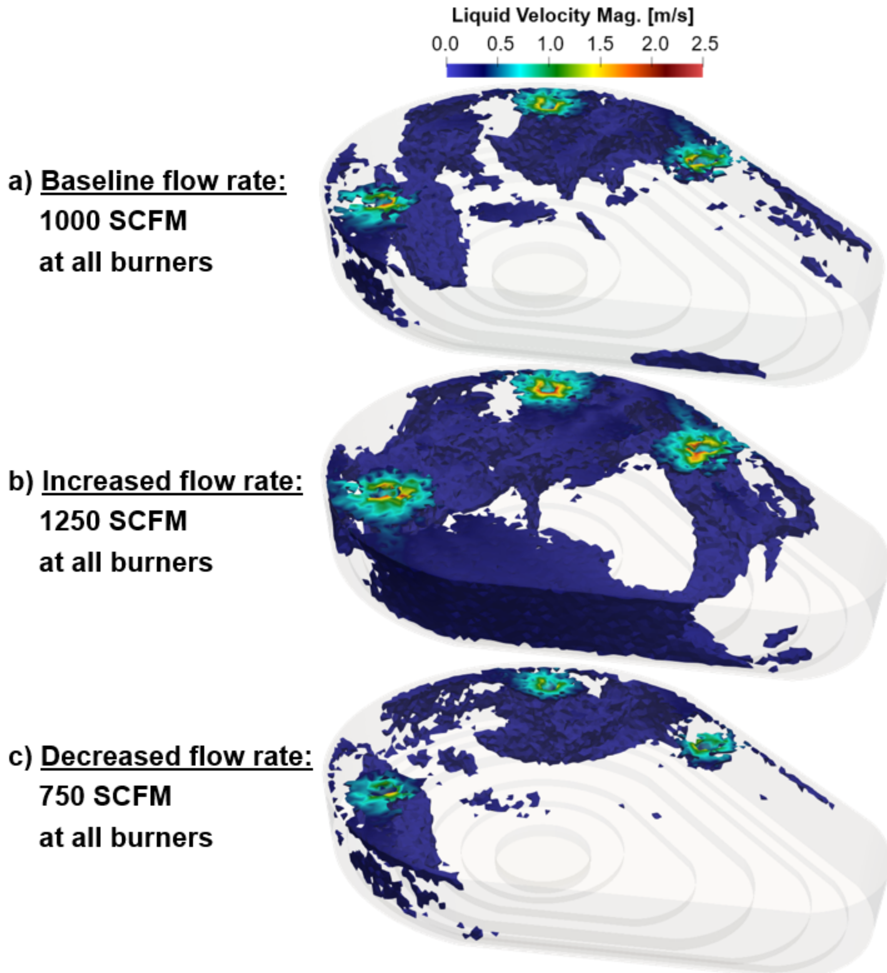

Figure 15. Regions where velocity magnitude is larger than 0.15m/s for baseline, increased and reduced flow cases

3.4.2 Impact of Individual non-uniform

The analysis performed in Section 3.4.1 is extended to include variations in the flow rate of the coherent jets by separate. This leads to non-uniform injection rate scenarios. Three cases are considered in this study, which are detailed in cases 1 through 3 in Table 3

Table 3. Case conditions for non-uniform flow rate parametric study

Cases	Coherent jet flow rates [SCFM]		
	Burner 1	Burner 2	Burner 3
1	750	1000	1250
2	1250	750	1000
3	1000	1250	750

Contours of the liquid velocities and flow vectors of the non-uniform injection scenarios at t = 600 s. are shown in Figure 16. In all these results, the flow rate injected by the three burners combined is the same, 3000 SCFM. However, the flow pattern varies significantly depending on the location of the burner that is increased or decreased respect to the baseline flow rate of 1000 SCFM. Figure 16b shows the case where the largest flow rates are at burners 2 and 3. In this case, the dead zone region is increased in the center of the furnace as compared to the baseline due to the stirring driven mainly by burners that are located opposite to each other. By increasing the flow rate in burner 1 and reducing it in burner 2, Figure 16c, the largest flow rates are injected near the top side of the plane, where burners 1 and 3 are located. This also increases the flow velocities near burner 2, even though the flow rate in this burner is reduced to 750 SCFM. In this case, the flow velocities are larger than in the baseline case, although a dead zone region is formed in the center of the domain in addition to the one formed at the balcony. Finally, by setting burners 1 and 2 to the largest flow rates while reducing the injection rate at the burner 3 (Figure 16d), the flow velocities are intensified as well, but the increasing of the flow velocities is mostly at the left side of the plane view, whereas the right side and balcony region are exposed to low liquid velocities.

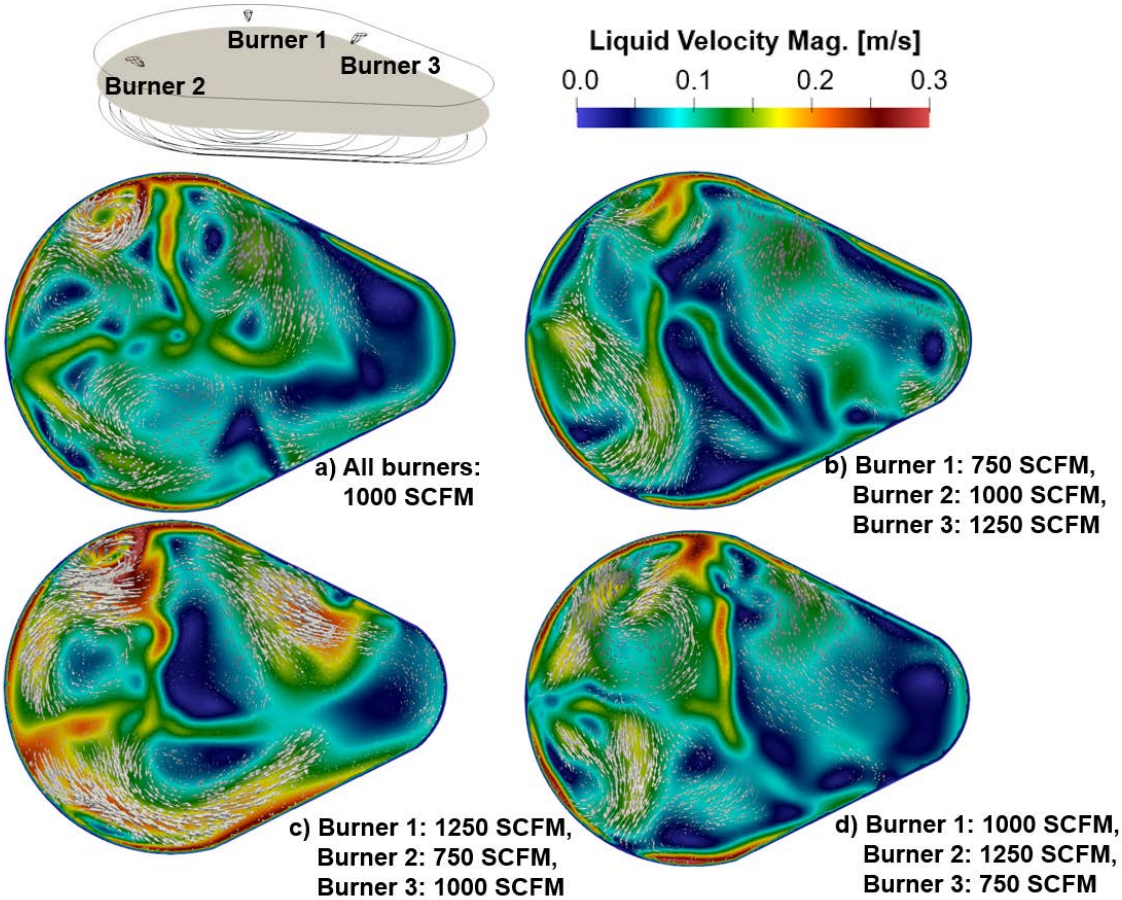

Figure 16. Velocity magnitude and flow vectors of baseline, and individually modified injection rate cases

Figure 17 compares the flow velocities of liquid steel at a plane taken along the furnace centerline, towards the balcony region. In all four cases, there is a ‘jet’ type flow from the liquid surface towards the bottom of the furnace near the center of the plane. The location of this jet flow changes with the flow rate of the burners. In Figure 17a and 17d, the jet flow is seen closer to the center of the plane than in Figures 16b and 16c. In all cases, flow recirculation is observed to the left of the jet flow. The location and intensity of the jet flow is expected to have a significant impact on the mixing process, which will be analyzed in the next section.

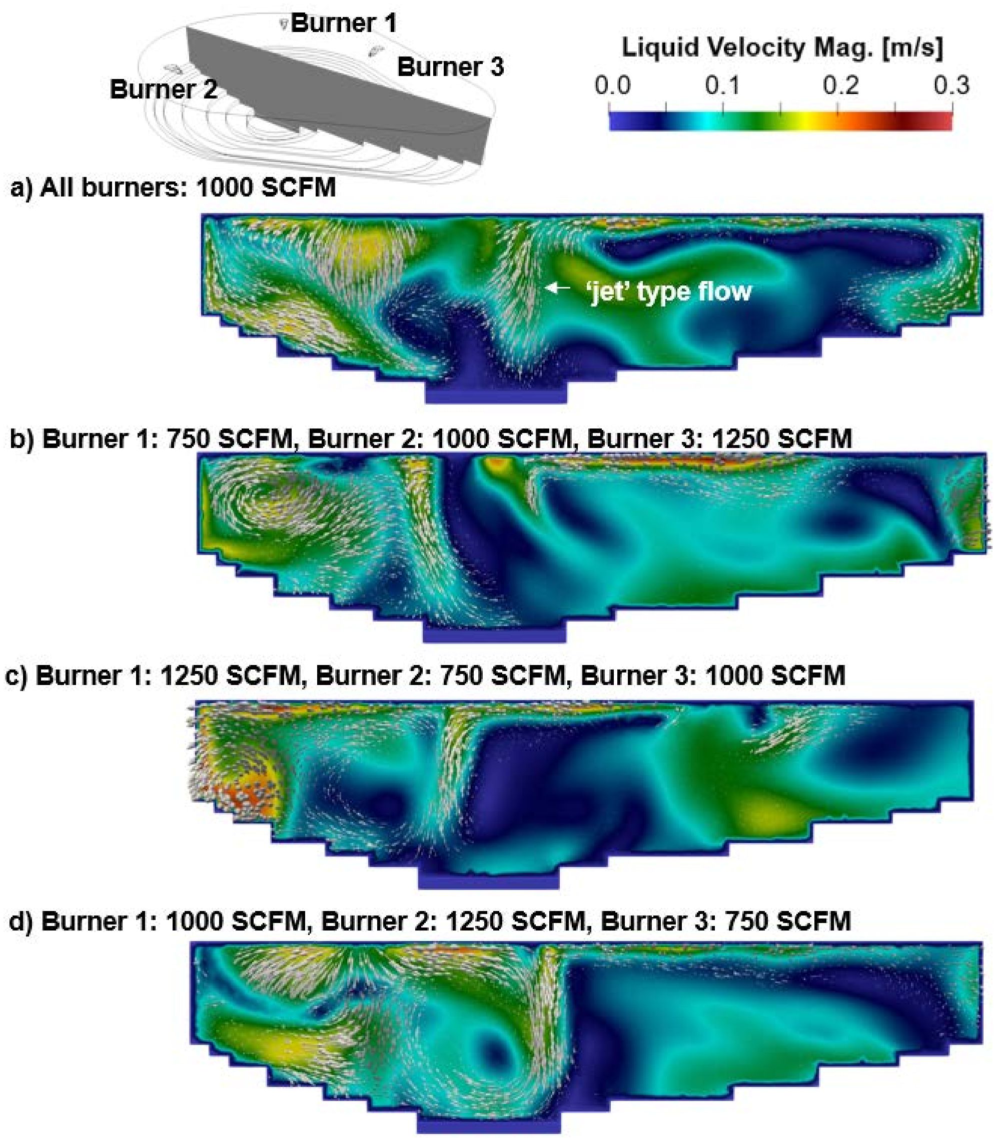

Figure 17. Velocity magnitude and flow vectors of baseline, and individually modified injection rate cases computed in vertical planes

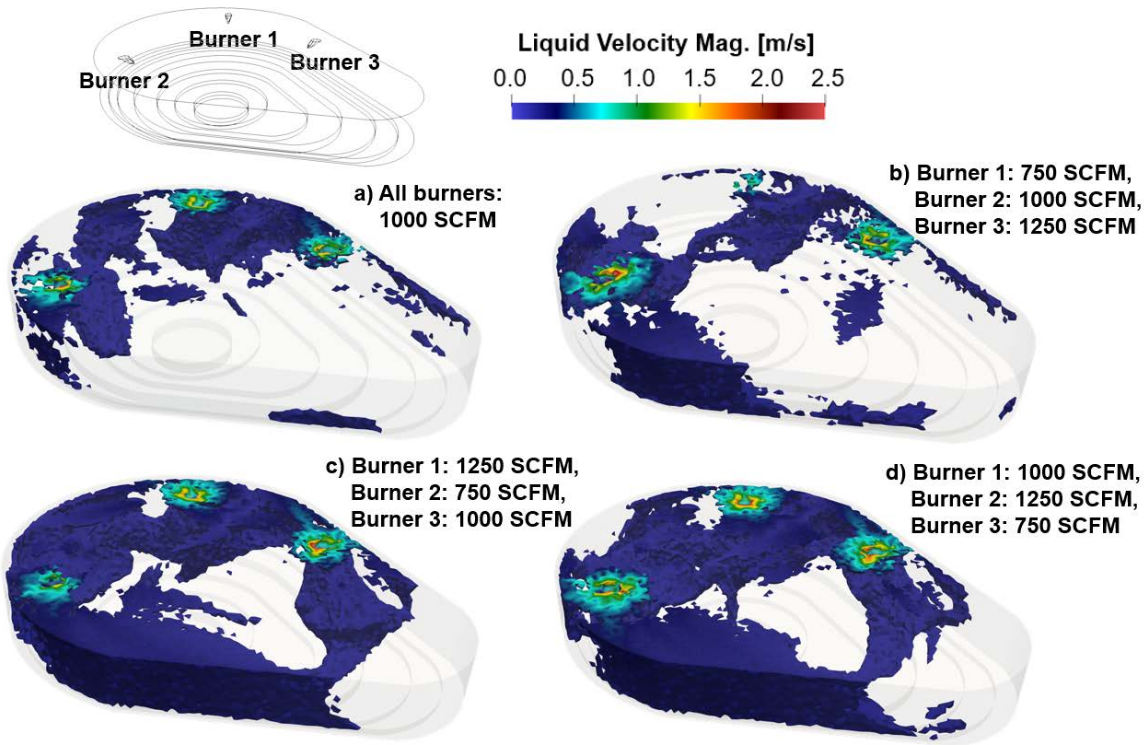

Figure 18. Regions where velocity magnitude is larger than 0.15 m/s for baseline, and individually modified injection rate cases

Figure 18 shows the regions where the liquid flow velocities are larger than 0.15 m/s for the cases listed in Table 3. As mentioned earlier, the total flow rate is the same for all the cases, but clearly the stirring intensity is not, as injection rate in each of the burners is modified. The largest flow intensities are seen in Figures 18c and 18d. In these two cases, the burners injecting the largest flow rates, 1000 and 1250 SCFM, are located next to each other. On the contrary, in Figure 18b, the largest flow rates are applied by burners opposite to each other (burners 2 and 3).

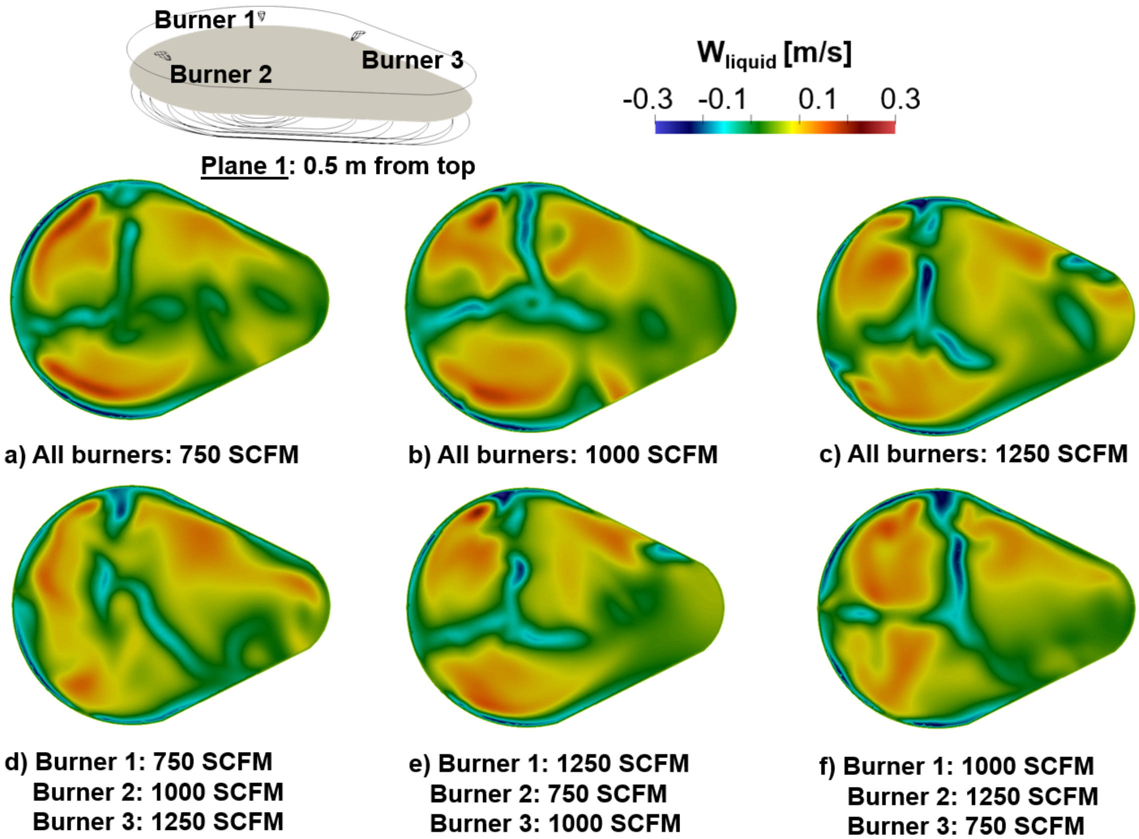

Figure 19. z component velocities computed near the bath surface for cases 1-6

The last set of results presented in this section corresponds to the *w* velocity computed 0.5 m. from the top of the domain, for all six cases presented in this study (Figure 19). The *w* velocity is the velocity component that is perpendicular to the surface of the liquid bath, and it is expected to have an impact on the reactions produced in the steel-slag interface and on the slag mixing. Figure 19 shows three regions in each of the cases where *w* is positive (flow moving towards the bath surface). These regions correlate with the locations of the burners. Interestingly, the case with the reduced flow injection (750 SCFM, Figure 19a) shows larger *w* velocities than the baseline case and the case with increased flow injection (Figure 19b and 19c, respectively). These larger *w* velocities are observed near the walls, adjacent to the burners. However, Figure 19a also shows the larger regions with negligible *w* velocity among the three uniform injection cases.

Figures 19d-f show the cases with non-uniform injection rates. Among these results, Figure 19d shows the case with the smallest region containing zero or near zero *w* velocities. The largest *w* velocities, however, are seen in Figure 19e. As mentioned earlier, the *w* velocity component is expected to impact the reactions near the steel/slag interface.

3.5 Discussion

In order to quantify the effect of the injection rates on the bath mixing, two parameters are defined, namely, the mixing time, which is the time needed by any species to blend into the generated flow, and the standard deviation of the fluid flow velocity, which determines the homogeneity of the velocity field in the liquid bath.

The mixing time is computed by introducing a passive tracer in the generated flow, with a mass fraction $Y_{tracer} = 1.0$. The uniformity index, which represents how a specified field variable varies over the domain, is used to calculate the mixing time. Specifically, the uniformity index is calculated as:

$$y_a = \frac{1}{V} \sum_{i=1}^{n} \emptyset_i \, |V_i| \tag{12}$$

Where $\bar{\emptyset}_i$ is the local value of the field variable. In this study, $\bar{\emptyset}_i$ is given by Y_{tracer}. According to this definition, a uniformity index of 1 indicates a uniform concentration of the passive tracer throughout the domain.

The local variation of the uniformity index with time can be obtained by calculating it at selected planes along the simulation. This requires computing the uniformity index in a per area basis rather than per volume as given by Equation 12. Figure 20 shows the uniformity variations with time of selected planes for the baseline case (1000 SCFM in all the burners). The planes where the uniformity index is computed at are shown on the right side of the figure. Results in Figure 20 show how the uniformity index varies in time with the selected location, and how the uniformity index value eventually converges to ~ 1 at a similar time for all planes, around 640 s. In the results to be discussed next, the mixing time in each of the cases is determined by the time where the uniformity index calculated in a per volume basis (by using Equation 12) reaches 0.95.

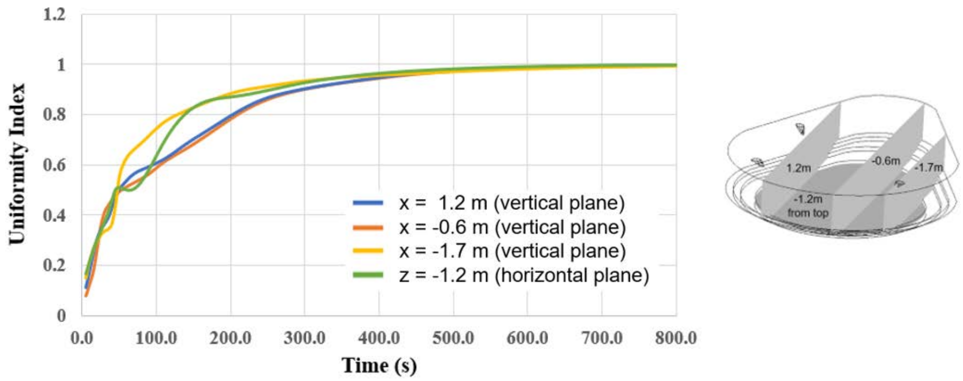

Figure 20. Local variations of uniformity index with time for baseline case

Figure 21 shows the mixing time for cases 1 (baseline, 1000 SCFM in all burners), 2 (1250 SCFM in all burners) and 3 (750 SCFM in all burners). This illustrates the effect of increasing and reducing the uniform flow rate of the coherent jet on the mixing process. Namely, a 25% increase in the flow rate leads to a reduction of 6.7% on the mixing time, whereas by reducing the uniform flow rate by 25%, the mixing time increases in 10.9%.

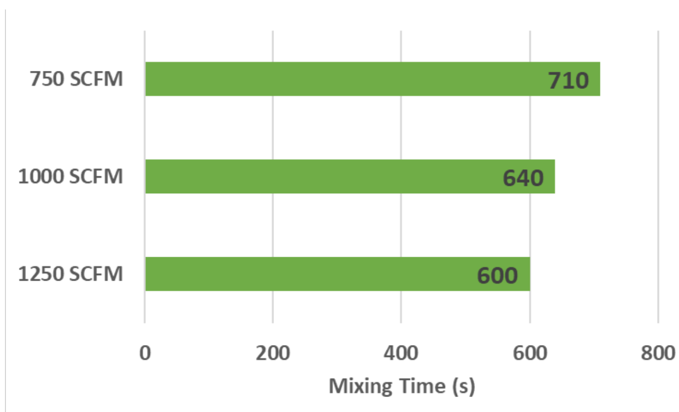

Figure 21. Mixing time for cases with uniform flow injection rates

Figure 22 compares the mixing times, standard deviation and decarburization of the baseline case and the cases with non-uniform injection rate at the burners (cases 1 through 3 in Table 3). Results show that the non-uniform injection rate cases reduce the mixing time obtained in the baseline case (green bars in Figure 22). This reduction is correlated with an increase in the standard deviation of the flow velocity respect to the baseline case (yellow bars in Figure 22).

Figure 22 also shows that the shortest mixing time does not correlate with the largest standard deviation of the flow velocity. Specifically, case 1 is the most optimal case as it reduces the mixing time the most: 10.2% respect to the baseline. Figure 16b showed that case 1 (burner 1=750 SCFM, burner 2=1000 SCFM, burner 3=1250 SCFM) prevented the formation of dead zones at the balcony region, and was able to continue stirring the flow in the center of the domain. Similarly, Figure 17b showed that case 1 reduced the dead zones, and promoted the flow penetration near the balcony region. Although case 1 did not lead to the most intense liquid flow field, the injection distribution in this case addressed the stirring of the central region of the furnace and the balcony region which, based on the multiple scenarios investigated, are the most difficult to stir.

Cases	Burner 1 SCFM	Burner 2 SCFM	Burner 3 SCFM	Mixing Time (s)	Uniformity	Decarburization
Base	1000	1000	1000	-	-	-
1	1250	1000	750	- 9 %	+ 3 %	- 5 %
2	750	1250	1000	- 6 %	+ 2 %	- 2 %
3	1000	750	1250	+ 2.2 %	+ 1.2 %	-2.6 %

Figure 22. Mixing time and standard deviation of velocity for baseline and cases with individually modified flow injection rates

3.6 Conclusion

In this study, a CFD platform has been used to analyze the stirring of molten steel driven by oxygen injection in an industry-scale EAF. A CFD platform was used to perform non-reacting, three-dimensional, transient simulations of the liquid bath as it interacts with three coherent jets operating in lance mode. The coherent jets are distributed in an asymmetric manner in the furnace. A baseline simulation is set based on operation conditions provided by EVRAZ North America. In this case, the coherent jets inject oxygen at 1000 SCFM in all the three burners. Results show that large fluid velocities near the burners drop significantly as the flow interacts with walls and flows injected from adjacent burners. The flow pattern is highly non-uniform due to the geometry of the furnace and the asymmetric distribution of the injectors. In the baseline case, flow recirculation develops near the burners, in particular near burner 1. Also, ‘dead zones’ develop at the balcony of the furnace, at the wall opposite to burner 3 and near the center of the domain. Analysis performed in vertical planes show large velocities near burners 1 and 2 (front of the furnace) and vertical recirculation also developing in this region.

The effect of injection rate on the stirring process is first studied by increasing and decreasing the injection rate in all burners respect to the baseline case. Namely, two injection cases are considered: 750 SCFM and 1250 SCFM in all burners. The increased flow rate strengthens the vortices formed in the vertical center plane of the furnace, whereas the reduced flow reduces the number of vortices developing in this direction. The impact of injection rates on the flow mixing is further studied by simulating three cases where the injection rate is modified in each burner, but the total flow rate is kept at 3000 SCFM. Results show that by keeping the largest injection rates at burners 2 and 3, opposite to each other, it is possible to reduce the dead zones in the balcony. Also, the individual injection rates modify the formation of the ‘jet’ type flow in the vertical direction, moving the jet flow towards the front of the furnace when the injection rate of any of the front burners (burners 1 and 2) is decreased.

The flow analysis of these cases is quantified by introducing two variables: the mixing time and the standard deviation of the flow velocity. The mixing time was computed based on the concentration of a passive tracer injected into the flow field. Results of the uniform injection cases show that mixing time reduces as the injection rate set in all the burners is increased. Namely, a 25% increase in the flow rate leads to a 6.7% reduction, whereas by reducing the uniform flow rate by 25% the mixing time increases in 10.9%. Moreover, the non-uniform injection rate cases improve the mixing obtained in the baseline case. Namely, the mixing time reduced 10.2% when the largest flow rates were set to coherent jets located opposite to each other in the furnace (burner 1=750 SCFM, burner 2=1000 SCFM, burner 3=1250 SCFM). Results also showed that the non-uniform injection cases increased the standard deviation of the flow velocities in the furnace respect to the baseline, which lead to an overall improvement on the stirring process and reduction of the time needed to reach a homogenous concentration field.

4. MELTING OF HBI IN AN EAF

4.1 Introduction

The melting stage in an EAF involves melting of recycled steel scrap to produce molten steel which is then refined to form a finished steel product. However, in an effort to reduce carbon emissions along with energy saving due to the increase in urgency of decreasing the spread of global warming. The significance of using HBI-DRI as a substitute for traditional scrap is the ability of HBI to conduct heat faster and this in turn shortens the time period of the entire melting thus conserving energy.

The objectives of this project are in order of effectively utilizing HBI to optimize the melting process:

- Development of scrap melting simulator to simulate melting of HBI-DRI in the EAF
    - Include chemical composition of scrap and its corresponding reactions
    - Draw relation for melting temperature of scrap based on carbon content
    - Involving feedback between evolved CO which reduces FeO present in HBI

The previously developed scrap melting simulator [20, 39] integrates the Electric Arc model along with the coherent jet model to serve as the 2 important heat sources required for the melting of scrap.

The Electric Arc model supplies the heat from the electrode, based on the power and voltage characteristics of a 3-phase electrode. This model also allows the electrode to perform a bore-in motion into the scrap, as it is melting, to replicate the real life scenario.

The Coherent jet model supplies heat in the form of a combustion reaction taking place between a fuel, Methane, and oxygen. These reactants are fed as a fixed premixed mixture into the eddy dissipation chemical reaction model, and upon combusting supply to the scrap via conduction and convection.

The flowchart of the models used is shown below:

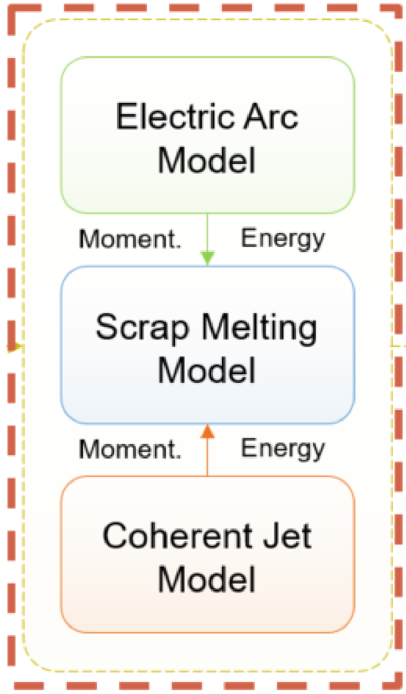

Figure 23. Integration of models used to form the Scrap Melting Simulator

4.2 Numerical Model

This section presents a brief summary of the CFD platform. Further details of the implementation and validation of the CFD solver can be found in [20, 39]. The melting of the HBI/scrap charge is accounted by three CFD models working together, namely, the scrap/HBI melting model, the electric arc model and the coherent jet model. Owing to the complex nature of the process, postulates to simplify the simulation are as follows:

1) CFD framework is based on the Finite Volume Method (FVM) with cell centered mass and heat transfer phenomenon.
2) The scrap and liquid steel undergoing the melting process maintain fixed physical properties such as density, characteristic diameter, specific heat, thermal conductivity and viscosity [33].
3) The porosity distribution is equal throughout the scrap/HBI layer of a given scrap/HBI type [34].

4) The scrap/HBI collapse is predominantly vertical in nature, i.e. it is modeled whilst neglecting random collapse at the periphery of the melting pit [35].
5) The load is identically shared across the three phases of the AC EAF circuit.
6) The slag formation in the liquid phase is not modeled in the current study.
7) The intra-gas phase emission and absorption of arc radiation is neglected. The propagation of radiation to solid scrap, liquid steel, furnace roof and walls are included.

4.2.1 Scrap Melting Model

Fluid phases

The liquid steel and gas phase are computed by using an Eulerian approach. The mass, momentum and energy equations are solved with source terms for mass conservation for liquid – solid mass transfer, momentum conservation for inter-phase interaction forces and momentum induced due to impingement of arc on liquid bath. The energy released by combustion reaction to the gas phase, along with the heat transfer from the arc and between the phases are included at the energy conservation equation. During the normal operation of EAF, the flow in the fluid experiences both high temperature and high speed hence, the standard k-ε turbulence model is used to simulate the turbulence within the fluid.

$$\frac{\partial(\alpha_q\rho_q)}{\partial t} + \nabla\cdot(\alpha_q\rho_q\vec{v}_q) = \dot{m}_{s,mt} \tag{17}$$

$$\frac{\partial(\alpha_q\rho_q\vec{v}_q)}{\partial t} + \nabla\cdot(\alpha_q\rho_q\vec{v}_q\vec{v}_q) = -\alpha_q\nabla p + \nabla\cdot\bar{\bar{\tau}}_q + \vec{F}_{q,df} + P_l + \alpha_q\rho_q\vec{g} \tag{18}$$

$$\begin{aligned}\frac{\partial(\alpha_q\rho_q E_q)}{\partial t} &+ \nabla\cdot\left(\alpha_q\vec{v}_q(\rho_q E_q + p)\right) \\ &= \nabla\cdot\left(K_{eff_q}\nabla T_q - \sum_{i=1}^{n} h_{i_g}\vec{J}_{i_g} + \bar{\bar{\tau}}_q\cdot\vec{v}_q\right) + Q_{q,ht} + Q_{l,arc}\end{aligned} \tag{19}$$

Solid phase

Solid scrap and HBI are referred to as solid phase. The solid phase is a porous medium modeled with a dual-cell approach to obtain dynamic collapsing of the solid undergoing the melting process. The dual cell approach is a finite volume-based approach which at the solid and fluid boundary uses the local energy balance and mass balance. The scrap porosity of each cell is updated based on the amount of mass transferred from the cell.

$$\frac{d(m_s)}{dt} = -\dot{m}_{s,mt} \tag{20}$$

$$\frac{d(E_s)}{dt} = \bar{\bar{Q}}_s \tag{21}$$

Phase Interactions

There are two different phase interactions in this model: the drag forces and energy exchange between the phases. The porous scrap pile induces a drag force on the fluid passing through it. This drag force is characterized by a pressure drop which is a high pore Reynolds number flow dictated by non-Darcian law [36]. Where the solid permeability and the inertial resistance are obtained by solving Ergun equation [37]. The heat transfer between each pair of phases is also calculated in conjunction with force interactions. In the current model, following previous research [38], the coefficient of convective heat transfer from liquid to solid phase is calculated for above-bath and in-bath condition separately. The coherent jet combustion flame plays an eminent part in solid melting by the solid – gas heat transfer and is elaborated in a later section.

$$h_{ls} = \begin{cases} \dfrac{\left(0.664{Re_{ls}}^{0.5}{Pr_l}^{0.333}\right)\lambda_l}{d_s} & (above - bath) \\ \dfrac{2\gamma\sqrt{Re_{ls}Pr_l}\lambda_l}{(1.55\sqrt{Pr_l} + 3.09\sqrt{0.372 - 0.15Pr_l})d_s} & (in - bath) \end{cases} \tag{22}$$

$$h_{gl} = \frac{\left(2 + 0.6{Re_{gl}}^{0.5}{Pr_g}^{0.333}\right)\lambda_g}{d_l} \tag{23}$$

Melting/Re-solidification

The melting and re-solidification is governed by the phase temperature and is achieved by liquid-solid mass transfer. In a given cell above or below a certain temperature, the mass is transferred in its entirety and the reversal direction of mass transfer is denoted by a negative sign.

$$\dot{m}_{s,mt} = \begin{cases} \dfrac{dm_s}{dt} & (T_s \geq T_{liquidus}) \\ -\dfrac{dm_l}{dt} & (T_l < T_{solidus}) \end{cases} \tag{24}$$

The effective specific heat capacity method with an assumption of constant temperature phase change was used to assign the latent heat of phase change.

$$C_{p,eff} = \begin{cases} C_{p,s} & (T < T_{solidus}) \\ C_{p,s} + \dfrac{h_{fusion}}{T_{liquidus} - T_{solidus}} & (T_{solidus} \leq T \leq T_{liquidus}) \\ C_{p,l} & (T > T_{liquidus}) \end{cases} \tag{25}$$

Scrap Collapse

The scrap collapse is achieved by a vertical stack methodology which ensures mass conservation during the process of scrap movement. For a given mesh the computational domain is usually made up of various vertical stacks. At the end of each time step, all the empty (gas) cells are marked in a given stack, the solid cells are then moved downward in steps until there are no empty cells below any solid cell thus achieving scrap collapse.

4.3 Model Development Methodology

HBI also known as Hot Briquetted Iron, is a form of Iron that is directly reduced from its ore. The premium advantage of using HBI instead of scrap, is that HBI offers quality improvements and can improve the productivity and efficiency of the furnace by the practice of continuous feeding.

When compared to standard scrap, HBI offers high carbon and metallic iron content however is very bulky and dense as well. As a result of this, if the heat supply to the HBI charged in the furnace is not good enough then they form clusters of metallic chunks that stick to the colder parts of the furnace and become more difficult to melt. Thus, more power is required initially to ensure sufficient heat is provided to melt HBI scrap and the goal is to minimize cold regions in the furnace. Once this important condition is sufficed and the HBI starts melting, it offers a decrease in its melting temperature as the melting cycle continues. The melting process of HBI is shown below.

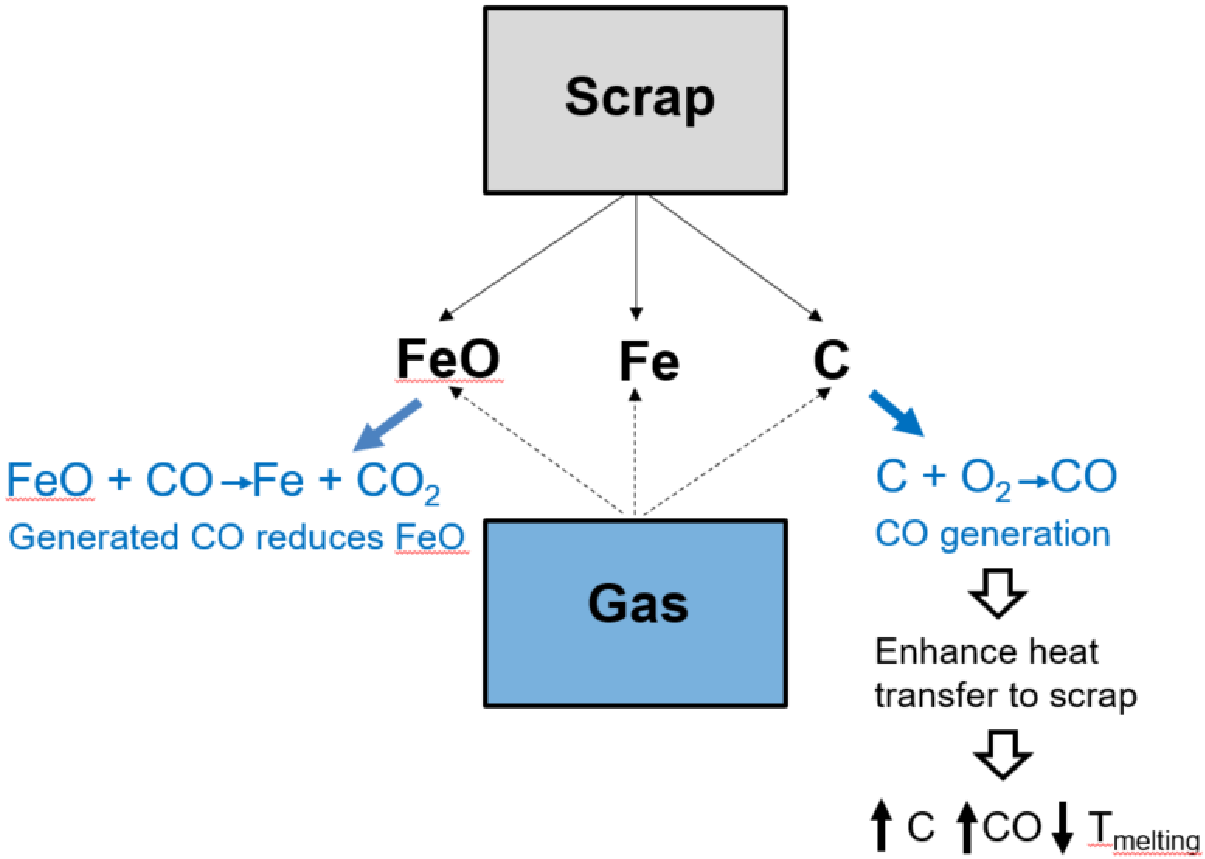

Figure 24. Stages of HBI melting

HBI consists of 3 major elements, which determine the quality of the product formed:

- Metallic Iron
- Unreduced Iron Oxide
- Carbon

The coherent jet burners provide oxygen to the furnace during the melting stage, which serves the purpose of combusting with the fuel to supply heat and also oxidizing the carbon present in the scrap to form carbon monoxide (CO) gas. This oxidation reaction is an exothermic reaction which releases heat and in turn aids in melting of the solid scrap.

At temperatures exceeding 600 C, the CO starts to react with the unreduced FeO to form metallic Fe and carbon dioxide. Additionally, the generation of CO greatly influences heat and mass transfer to the solid phase via natural convection, thus facilitating melting. The heat transfer coefficient is associated with the rate at which the gas is evolved [29].

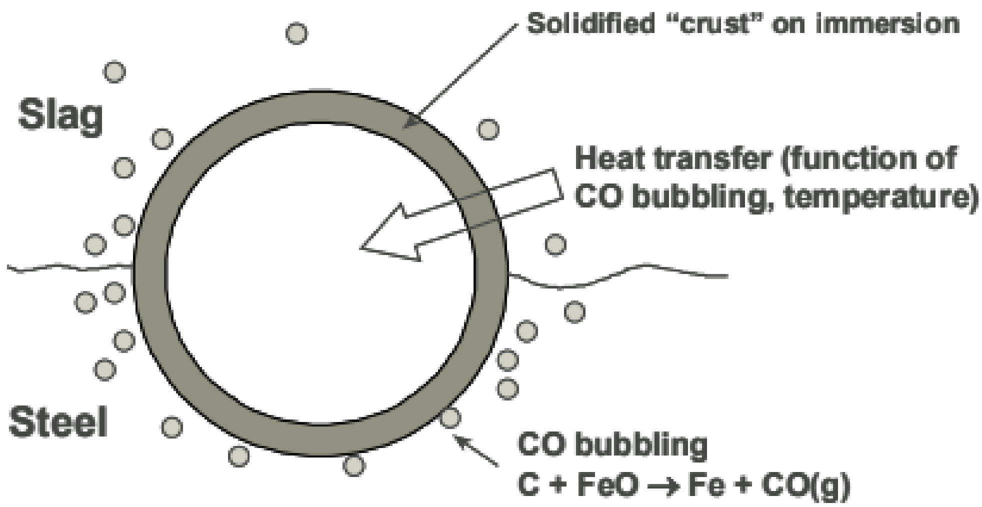

Figure 25. HBI melting process [27]

The overall reaction thus formed is one that of Carbon reacting with unreduced Iron Oxide to form Metallic Iron and Carbon Monoxide, which is broken down in the simulation to capture the accurate physics and chemistry of HBI melting.

The scrap melting simulator initially just captured the physical characteristics of the scrap in order to simulate melting. The primary factors for melting were density, porosity and melting temperature of the scrap. The addition to this model was done to further include the chemical composition of the scrap, the reactions involved and the impact of these on the heat transfer and melting associated with the scrap. The methodology simulated via the code, implemented via a User-defined Function (UDF) into ANSYS Fluent, is shown below:

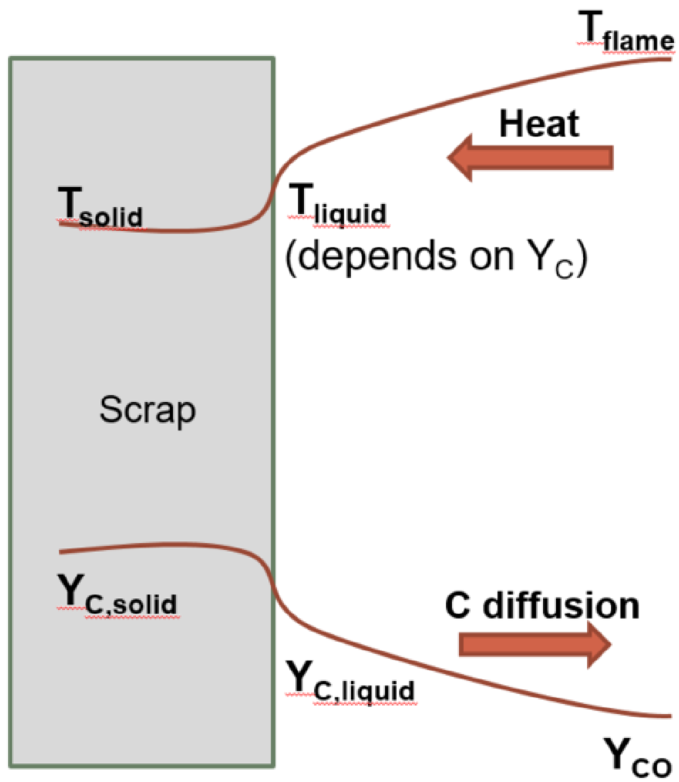

Figure 26. Melting Simulator methodology

The way the inclusion of chemical components and their reaction was done, was by writing mass and energy balance equations for each element respectively.

The solid phase conservation reactions are shown below:

$$\frac{dm_c}{dt} = -K_r.\dot{m}_c \tag{13}$$

$$\frac{dm_{Fe}}{dt} = \dot{m}_{Fe} \tag{14}$$

Where $\dot{m}_c$ is the instantaneous rate of change of mass of carbon, K_r is the rate of the reaction and $\dot{m}_{Fe}$ is the instantaneous rate of change of mass of Iron (Fe). The gas phase conservation reactions are written as shown below:

$$\frac{dm_{O2}}{dt} = -K_r.\dot{m}_c.\frac{16}{12} \tag{15}$$

$$\frac{dm_{CO}}{dt} = -K_r.\dot{m}_c.\frac{28}{12} \tag{16}$$

The gaseous mass balance equations are calculated based on the chemical equilibrium of reactions of Carbon and Iron oxide taking place.

4.4 Computational Domain and Grid

The Electric Arc Furnace used for this project had dimensions provided by NLMK. The furnace is an AC furnace and consists of 4 coherent jet burners, and 3-phased electrodes.

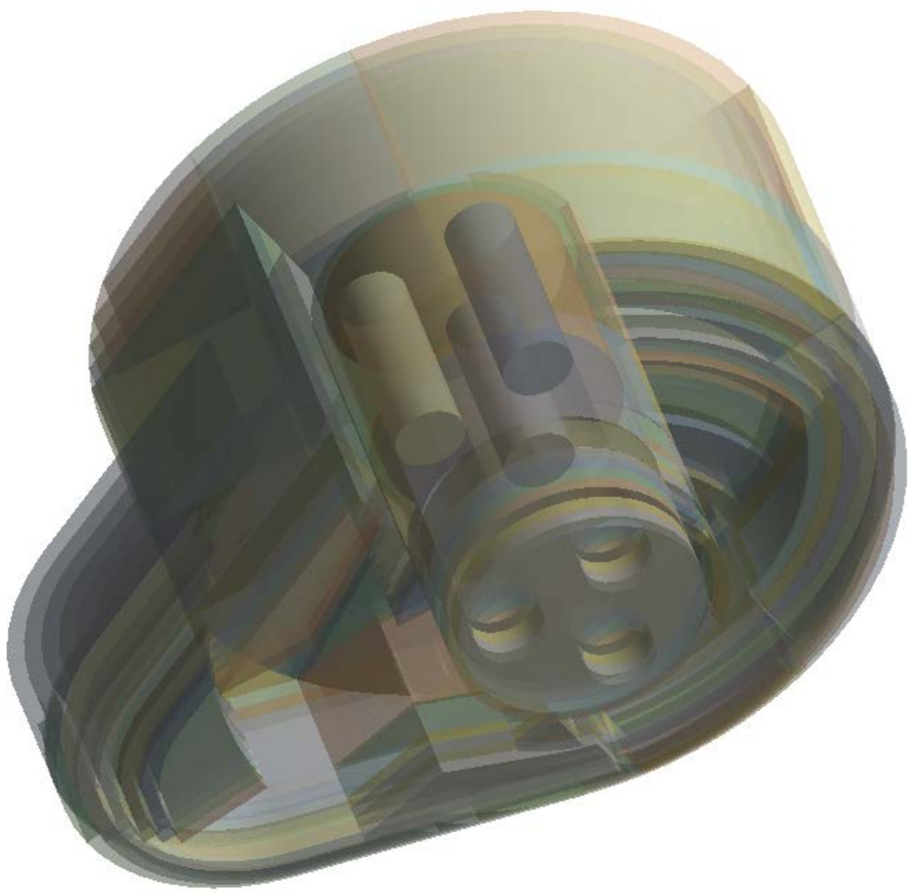

Figure 27. Geometry of an EAF

The geometry was designed using ANSYS design modeler.
The grid generated for the geometry of this EAF has to be such that all cells in the vertical direction have to be one below each other. This is owed to the dual cell methodology of simulating the virtual collapse of solid scrap phase into liquid phase.

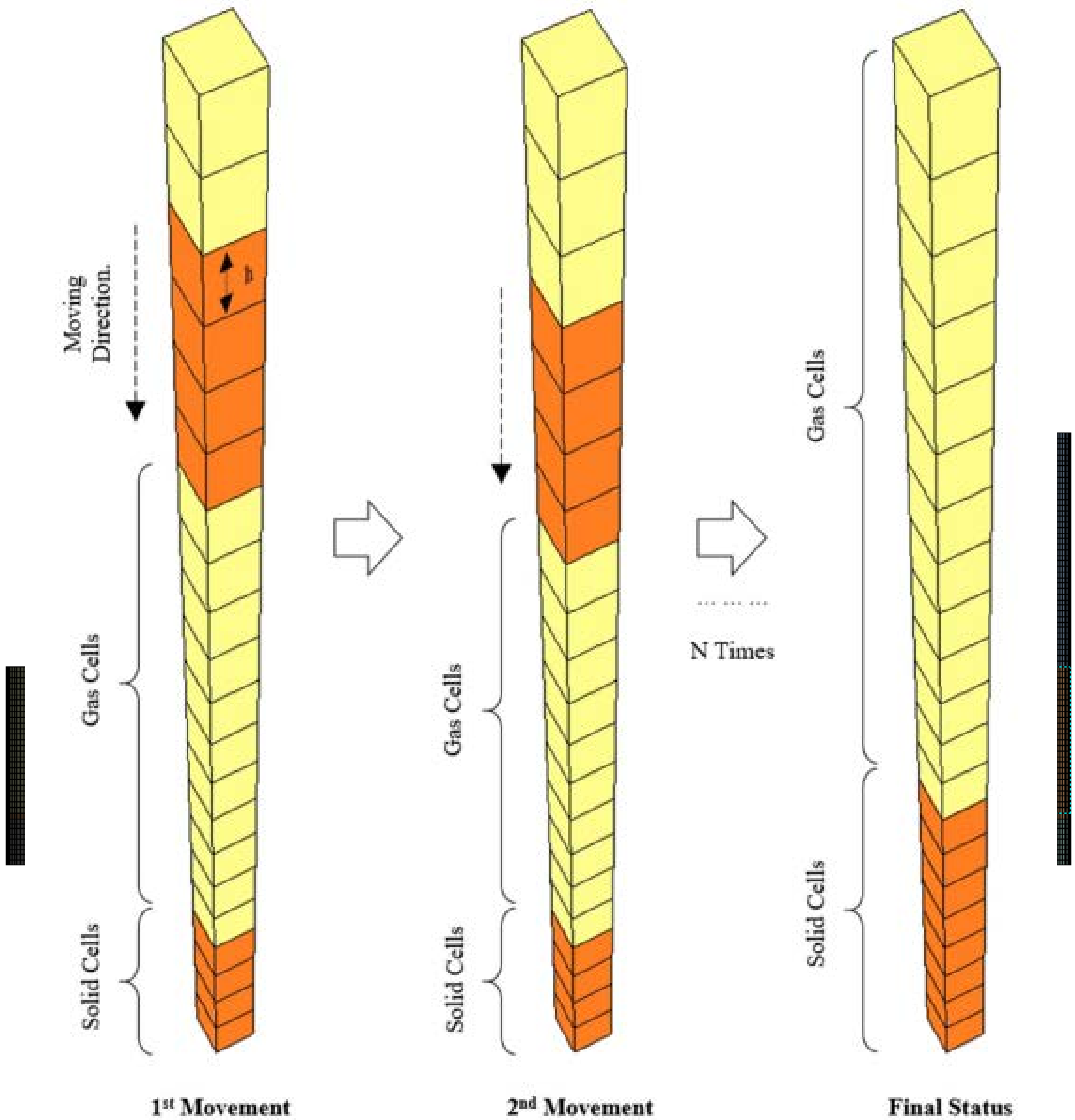

Figure 28. Dual cell collapse approach [20]

This method of scrap melting states that as the cells in the upper layers of the solid phase reach a certain temperature, the value of the volume fraction in these cells transfer from solid phase to liquid phase. As this happens, the cells transfer the value of the solid volume fraction to the cells below, and so on. This virtually denotes melting of layers whose temperature value has reached the melting threshold.

The mesh of the furnace as shown above, displays that all elements are roughly the same size and are below a threshold of 2 mm in the vertical direction. This is to ensure smoother transition of the dual cell melting phenomena and thus accurately capturing the physics of melting.
Similarly the mesh when seen from above, in a wireframe mode, confirms that no cells overlap the ones below them and that the transitioning never goes above 1.5 of its neighboring cell.

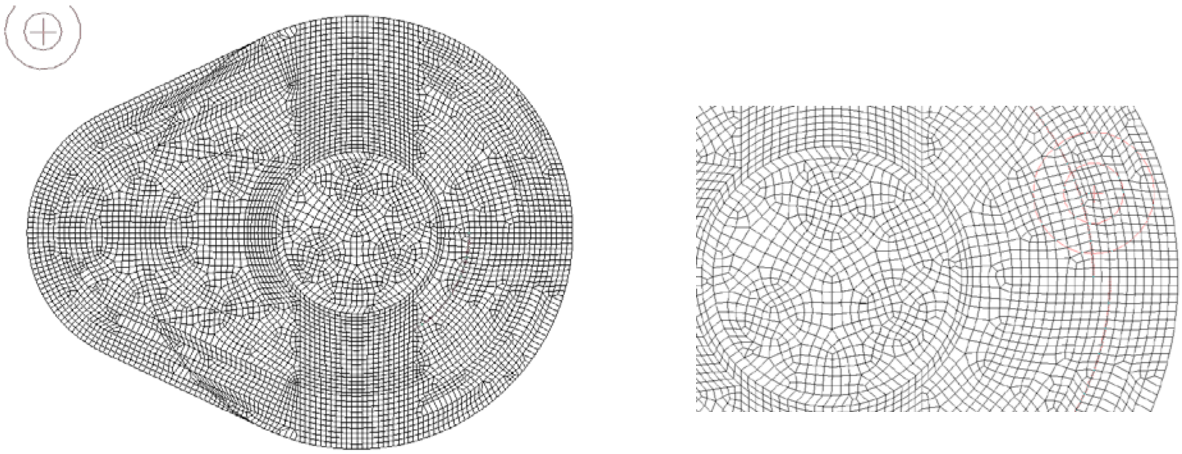

Figure 29. Wireframe top view of Mesh

4.5 Baseline Setup

The boundary conditions used for the baseline case are as shown below:

Table 4. Baseline Case conditions for HBI melting study

Number of Burners	4
Initial volume of charged material	72.2 m^3
Operation time	700 sec.
Scrap bulk density	0.9 T/m^3
HBI bulk density	2.4 T/m^3
Burner Power [MW]	3.2
Amp. Set Point [kA]	55
Nominal Voltage [V]	600

The data used for setting the power and voltage of the electric arc versus time is provided by NLMK for operation purposes.

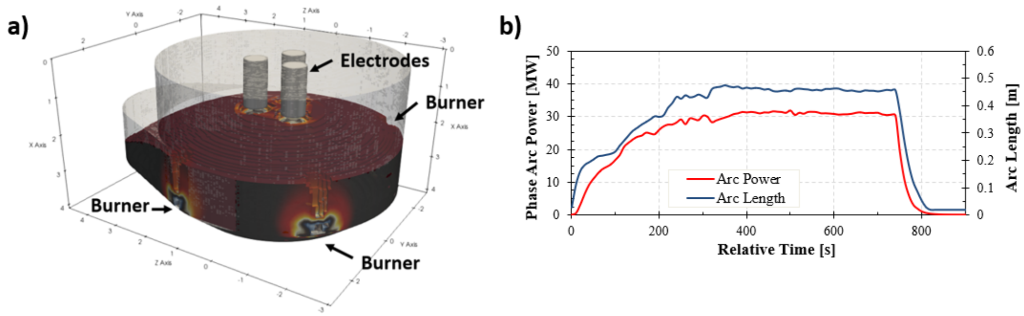

Figure 30. a) Scrap charged in domain b) Electrode data

4.6 Baseline Results

Figure 31 shows results of scrap melting for 2 species, Carbon and Fe, for 600 s of phase time. 25 % of the scrap melts after 600 s which is a 10 % reduction in time as compared to traditional scrap.

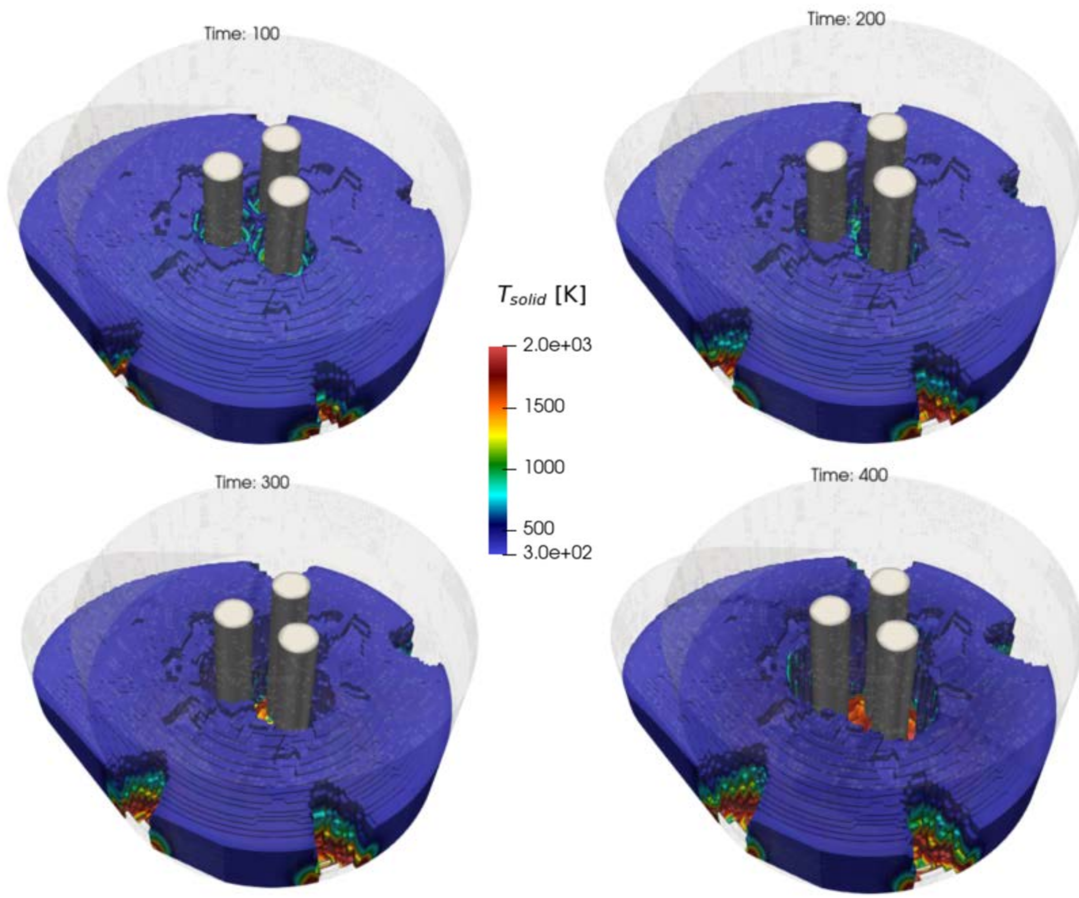

Figure 31. Melting of HBI over time

The electrode bore down phase takes about 300 s. Under the effect of arc radiation and convection, a proportionally small amount of scrap is melted in the first 300 s. The four burners provide heat and melt the scrap simultaneously from the surrounding cold spots. Approximately 8.9 % of the scrap is melted in the first 300 s of arcing and burning.

The main melting phase (300 – 600 s) follows after the initial bore-down phase. Arc radiation and flame convection during this phase significantly increase the center electrode pit and the surrounding burner melting chambers. As this is happening, the arc continues to heat the bottom liquid bath, melting the scrap pile as a result of the hot liquid bath's heat. This causes the upper scrap to have insufficient support, further forcing the scrap to collapse.

Figure 32 quantitatively depicts the previously mentioned scrap melting process, including the remaining scrap mass and the current electrode location. As can be observed, the electrode bore-down phase melts at a significantly slower pace than the main melting phase. This is due to the fact that the majority of the liquid steel that forms beneath the electrode drips downward into direct contact with the cold scrap and gas, gradually re-solidifying along the path. As a result, during the electrode bore-down phase, the liquid steel combines with the liquid bath instead of falling directly to the bottom of the furnace.

Figures 32 and 33 indicate the rate of melting of the solid phase and rate of CO formation.
As electrodes start to deepen down more of the solid phase is seen melting, this function is called the scrap collapse. It is based on the dual cell approach. Most of the melting is seen near the electrodes and the 4 coherent jet burners. The temperature of the melted scrap is also evidently high, around 1900 K.

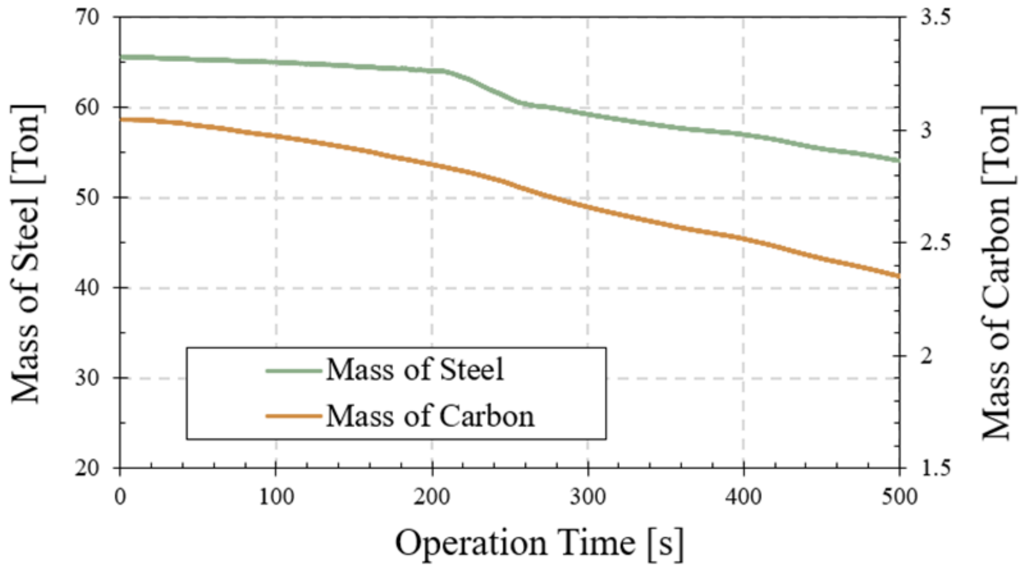

Figure 32. Melting rate of total solid mass

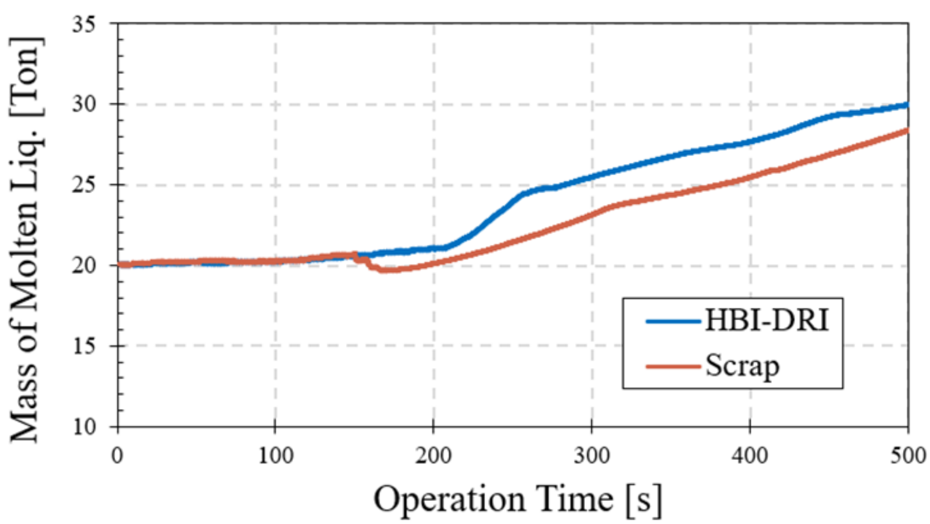

Figure 33. Rate of liquid steel formation

Molten bath mass increases at a faster rate for HBI/DRI as compared to traditional scrap due to its ability to melt faster owing to higher bulk density, better thermal and electrical conductivity. The heat produced via the oxidation reaction taking place, between carbon present in the HBI scrap and oxygen provided by the burners, also provides a good source and aids in further increasing the melting rate. As a result, for the same period of time, molten mass for HBI/DRI scrap is up to 11 % higher compared to traditional scrap.

4.7 Conclusion

The results from the extended scrap melting simulator, which replicates the scrap melting stage—that is, the melting of the scrap using both an AC electric arc and a coherent jet burner in an industry-scale EAF—are presented in this section. For the first time, the experimental validations of the scrap melting by arc were devised and implemented for the 150-ton NLMK EAF, which is used in industry, as presented by my mentor Yuchao Chen [20]. The physical concepts involved in melting of HBI were investigated using the simulator, and the following key findings were reached:

- The previously developed scrap melting model, which originally performed scrap melting by just taking into account the physical properties of the scrap, can now also handle solving the specific mass and energy balance equations for each individual element that is part of the steel chemistry and also simulate the appropriate reactions taking place during the melting stage.
- An accurate depiction of, previously validated data of charging 100 % traditional scrap in a furnace against current simulation of charging 100 % HBI as scrap in a furnace, was visualized and the results were analyzed to describe the impact of HBI on the melting process.
- Simulating the reactions involved during melting along with the actual melting phenomena can lead to a further analysis of how we could optimize the melting stage and potentially aid in energy saving. The current results show us that using HBI could potentially lead to a 11 % reduction in the melting process time which in turn leads to a huge chunk of resources conserved in terms of energy and work.

REFERENCES

[1] Oda, J., Akimoto, K., & Tomoda, T. (2013). Long-term global availability of steel scrap. Resources, conservation and recycling, 81, 81-91.

[2] Satyendra, (2015). Understanding Electric Arc Furnace Steelmaking Operations. Ispat Guru.

[3] Green Car Congress (2022). Steelmaking by EAF causes 75 % less carbon emissions. CRU Group.

[4] Nucor Newsroom (2019).

[5] Electric Arc Steelmaking – Brittanica.

[6] H. J. Odenthal, A. Kemminger, F. Krause, L. Sankowski, N. Uebber, N. Vogl, "Review on Modeling and Simulation of the Electric Arc Furnace (EAF)," Steel Res. Int., vol. 89, No. 1 (2018), pp. 17-98.

[7] Y. Li, W. T. Lou, and M. Y. Zhu. Ironmak. Steelmak., 2013, vol. 40, pp. 505-514.

[8] T. G. Kang, and P. D. Anderson. Micromachines, 2014, vol. 5, pp. 1270-1286.

[9] R. H. Liu, M. A. Stremler, K. V. Sharp, M. G. Olsen, J. G. Santiago, R. J. Adrian, H. Aref, D. J. Beebe. J. Microelectromech. Syst., 2000, vol. 9, pp. 190–197.

[10] Y. B. Duan and J. H. Wei. Shanghai Metals, 2007, vol. 29, pp. 31–36.

[11] E. Lang, P. Drtina, F. Streiff, and M. Fleischli. Int. J. Heat Mass Transfer, 1995, vol. 38, pp. 2239-2250.

[12] D. Mazumdar and R. I. Guthrie. Metall. Mater. Trans. B, 1986, vol. 17, pp. 725-733.

[13] M. Y. Zhu, T. Inomoto, I. Sawada and T. C. Hsiao. ISIJ Int., 1995, vol. 35, pp. 472-479.

[14] A. M. Amaro-Villeda, M. A., Ramirez-Argaez and A. N. Conejo. ISIJ Int., 2014, vol. 54, pp. 1-8.

[15] R. Cheng, L. Zhang, Y. Yin and J. Zhang. Metals, 2021, vol. 11, pp. 369.

[16] Y. Chen, A. K. Silaen, and C. Q. Zhou. Processes, 2020, vol. 8, pp. 700.

[17] S. Jayaraj, S. Kang, and Y. K. Suh. J. Mech. Science Tech., 2007, vol. 21, pp. 536-548.

[18] B. Li. ISIJ Int., 2000, vol. 40, pp. 863-869.

[19] Midrex (2021). HBI Steel's most versatile metal: Part 3.

[20] Chen, Y., Ryan, S., Silaen, A. K., & Zhou, C. Q. (2022). Simulation of Scrap Melting Process in an AC Electric Arc Furnace: CFD Model Development and Experimental Validation. Metallurgical and Materials Transactions B, 53(4), 2675-2694.

[21] Gonzalez, O. J. P., Ramírez-Argáez, M. A., & Conejo, A. N. (2010). Mathematical modeling of the melting rate of metallic particles in the electric arc furnace. ISIJ international, 50(1), 9-16.

[22] Caffery, G., Rafiei, P., Honeyands, T., Trotter, D., & Marketing, B. B. (2004, September). Understanding the melting characteristics of HBI in iron and steel melts. In AISTECH-CONFERENCE PROCEEDINGS- (Vol. 1, p. 503). ASSOCIATION FOR IRON & STEEL TECHNOLOGY.

[23] Dutta, S. K., & Sah, R. (2016). Direct reduced iron: Production. Encyclopedia of Iron, Steel, and Their Alloys; Colás, R., Totten, GE, Eds, 1082-1108.

[24] Morales, R. D., Rodriguez-Hernandez, H., Vargas-Zamora, A., & Conejo, A. N. (2002). Concept of dynamic foaming index and its application to control of slag foaming in electric arc furnace steelmaking. Ironmaking & steelmaking, 29(6), 445-453.

[25] Kiasaraei, E. S. (2010). Decarburization and Melting Behavior of Direct-reduced Iron Pellets in Steelmaking Slag. University of Toronto (Canada).

[26] Kirschen M, Hay T, Echterhof T. Process Improvements for Direct Reduced Iron Melting in the Electric Arc Furnace with Emphasis on Slag Operation. *Processes*. 2021; 9(2):402.

[27] Alameddine, S., & Bowman, B. (2008). Particularities of Melting DRI in AC and Dc arc furnaces. Archives of Metallurgy and Materials, 53(2), 411-417.

[28] Anderson, S. H. (2002, May). Educated use of DRI/HBI improves EAF energy efficiency and yield and downstream operating results. In 7th European Electric Steelmaking Conference & Expo, AIDM, Venice.

[29] M. Sano and K. Mori. Trans. Iron Steel Inst. Jpn., 1983, vol. 23, pp. 169-175.

[30] R. B. Banks and D. V. Chandrasekhara. J. Fluid Mech.., 1963, vol. 15, pp. 13-34.

[31] H. Ishikawa, S. Mizoguchi and K. Segawa. ISIJ Int., 1972, vol. 58, pp. 76-84.

[32] O. J. P. Gonzalez, M. A. Ramírez-Argáez, and A. N. Conejo, ISIJ Int., 2010, vol. 50, pp. 1-8.

[33] Opitz, F., & Treffinger, P. (2016). Physics-based modeling of electric operation, heat transfer, and scrap melting in an AC electric arc furnace. Metallurgical and Materials Transactions B, 47, 1489-1503.

[34] Chen, Y., Luo, Q., Silaen, A. K., & Zhou, C. Q. (2020). Multi-physics modeling of steel ingot melting by electric arc plasma and its application to electric arc furnace. Frontiers in Materials, 7, 576831.

[35] Guo, D., & Irons, G. A. (2008). Modelling of steel scrap movement. Applied mathematical modelling, 32(10), 2041-2049.

[36] Kladias, N., & Prasad, V. (1991). Experimental verification of Darcy-Brinkman-Forchheimer flow model for natural convection in porous media. Journal of thermophysics and heat transfer, 5(4), 560-576.

[37] Ergun, S. (1952). Fluid flow through packed columns. Chem. Eng. Prog., 48(2), 89-94.

[38] Austin, P. R., Nogami, H., & Yagi, J. I. (1997). A mathematical model for blast furnace reaction analysis based on the four fluid model. ISIJ international, 37(8), 748-755.

[39] Chen, Y. (2022). Integrated Multi-physics Modeling of Steelmaking Process in Electric Arc Furnace (Doctoral dissertation, Purdue University Graduate School).